Contrib Mineral Petrol
DOI 10.1007/s00410-009-0409-2

ORIGINAL PAPER

On the occurrence, trace element geochemistry, and crystallization history of zircon from in situ ocean lithosphere

Craig B. Grimes · Barbara E. John · Michael J. Cheadle · Frank K. Mazdab · Joseph L. Wooden · Susan Swapp · Joshua J. Schwartz

Received: 17 November 2008 / Accepted: 24 April 2009

Abstract We characterize the textural and geochemical features of ocean crustal zircon recovered from plagiogranite, evolved gabbro, and metamorphosed ultramafic host-rocks collected along present-day slow and ultraslow spreading mid-ocean ridges (MORs). The geochemistry of 267 zircon grains was measured by sensitive high-resolution ion microprobe-reverse geometry at the USGS-Stanford Ion Microprobe facility. Three types of zircon are recognized based on texture and geochemistry. Most ocean crustal zircons resemble young magmatic zircon from other crustal settings, occurring as pristine, colorless euhedral (Type 1) or subhedral to anhedral (Type 2) grains. In these grains, Hf and most trace elements vary systematically with Ti, typically becoming enriched with falling Ti-in-zircon temperature. Ti-in-zircon temperatures range from 1,040 to 660°C (corrected for $\mathbf{a}_{TiO2} \approx 0.7$, $\mathbf{a}_{SiO2} \approx 1.0$, pressure ≈ 2 kbar); intra-sample variation is typically ~60–150°C. Decreasing Ti correlates with enrichment in Hf to ~2 wt%, while additional Hf-enrichment occurs at relatively constant temperature. Trends between Ti and U, Y, REE, and Eu/Eu* exhibit a similar inflection, which may denote the onset of eutectic crystallization; the inflection is well-defined by zircons from plagiogranite and implies solidus temperatures of ~680–740°C. A third type of zircon is defined as being porous and colored with chaotic CL zoning, and occurs in ~25% of rock samples studied. These features, along with high measured La, Cl, S, Ca, and Fe, and low $(Sm/La)_N$ ratios are suggestive of interaction with aqueous fluids. Non-porous, luminescent CL overgrowth rims on porous grains record uniform temperatures averaging 615 ± 26°C (2SD, $n = 7$), implying zircon formation below the wet-granite solidus and under water-saturated conditions. Zircon geochemistry reflects, in part, source region; elevated HREE coupled with low U concentrations allow effective discrimination of ~80% of zircon formed at modern MORs from zircon in continental crust. The geochemistry and textural observations reported here serve as an important database for comparison with detrital, xenocrystic, and metamorphosed mafic rock-hosted zircon populations to evaluate provenance.

Communicated by H. Keppler.

Electronic supplementary material The online version of this article (doi:10.1007/s00410-009-0409-2) contains supplementary material, which is available to authorized users.

C. B. Grimes · B. E. John · M. J. Cheadle · S. Swapp
Department of Geology and Geophysics,
University of Wyoming, Laramie, WY 82071, USA

F. K. Mazdab · J. L. Wooden
U.S.G.S.-Stanford Ion Microprobe Laboratory,
367 Panama Mall, Stanford, CA 94305, USA

J. J. Schwartz
Department of Geological Sciences, University of Alabama,
870338, Tuscaloosa, AL 35487, USA

C. B. Grimes (✉)
Department of Geology and Geophysics,
University of Wisconsin, 1215 West Dayton Street,
Madison, WI 53706, USA
e-mail: cgrimes@geology.wisc.edu

Introduction

Zircon (nominally $ZrSiO_4$) is an invaluable tool in countless geologic studies due to its wide distribution in a spectrum of rock types, and the incorporation and retention of radiogenic isotopes amenable to age determination. In addition, zircon concentrates a plethora of trace elements

Published online: 19 May 2009

and preserves stable isotopic compositions, and can be used as an indicator of provenance (e.g., Heaman et al. 1990; Hoskin and Ireland 2000; Belousova et al. 2002; Grimes et al. 2007), terrestrial and lunar differentiation and maturation (e.g., Valley et al. 2005; Harrison et al. 2005; Nemchin et al. 2006), crystallization temperature (e.g., Watson and Harrison 1983, 2005), and the partitioning of trace elements from magmas during zircon formation (e.g., Sano et al. 2002; Thomas et al. 2002; Rubatto and Hermann 2007; Hanchar and van Westrenen 2007 and references therein). The application of zircon geochemistry to investigate geologic processes therefore extends beyond geochronology. Recent advances have come in large part from the development of high precision analytical techniques that allow detailed, micron-scale evaluation on single crystals.

Zircon is most common in continental igneous rocks with intermediate to silica-saturated compositions (Hoskin and Schaltegger 2003), but it has also been reported at low abundance in mafic rocks (e.g., Scoates and Chamberlain 1995; Hoskin and Ireland 2000; Belousova et al. 2002), kimberlite (e.g., Kreston et al. 1975; Konzett et al. 1998), carbonatite (e.g., Heaman et al. 1990; Hanchar and Hoskin 1998), and in rocks formed by hydrothermal processes (e.g., Hoskin and Schaltegger 2003, and references therein; Hoskin 2005). It is also evident that the formation of zircon is not isolated to continental settings. Zircon has been used to date numerous ophiolites (e.g., Mattinson 1976; Tilton et al. 1981; Mukasa and Ludden 1987; Warren et al. 2005), and is recognized within plutonic intervals of in situ ocean crust formed over a range of spreading rates. Differentiated plutonic rocks host to zircon have been sampled along the ultra-slow spreading Southwest Indian Ridge (SWIR) (e.g., Robinson et al. 2002; John et al. 2004; Schwartz et al. 2005; Reddy et al. 2006; Baines et al 2008), slow-spreading Mid-Atlantic Ridge (MAR) (e.g., Cannat and Casey 1995; Cannat et al. 1997a; Kelemen et al. 2004; Schroeder and John 2004; Moeller et al. 2006; Grimes et al. 2007; Hellebrand et al. 2007; Cavosie et al. 2009; Jöns et al. 2009; Lissenberg et al. 2009), and fast spreading East Pacific Rise (e.g., Gillis 1996; Coogan and Hinton 2006). Zircon has also been reported in dacite recovered from the intermediate-spreading Juan de Fuca Ridge (Cotsonika et al. 2005).

Following the application of zircon geo- and thermochronometry by John et al. (2004) to study in situ ocean crust, the appreciation of the importance of zircon in this setting has grown. For example, apart from the new chronologic constraints zircon provides, ocean crustal zircons place constraints on the origin of the Earth's oldest known detrital zircons (e.g., Coogan and Hinton 2006; Grimes et al. 2007). Coogan and Hinton (2006) suggested that, on the basis of Ti and REE chemistry, detrital grains in the Jack Hills (Australia) could have been derived from oceanic crust, and hence preclude the need for the >4.0 Ga proto-continental crust (e.g., Harrison et al. 2005; Valley et al. 2005; Watson and Harrison 2005). However, using primarily U and Yb concentrations, Grimes et al. (2007) developed discrimination diagrams that effectively distinguished 80% of modern ocean crustal zircons from continentally-derived zircons, noting that the vast majority of >4.0 Ga detrital zircons plot in the exclusively continental field. Given the emphasis placed on zircon in many geologic studies (extending beyond even the rock record), comprehensive characterization of the geochemical composition of modern ocean zircon is critical for comparison with xenocrystic, detrital, and other out-of-context zircon populations, as well as eclogite and ophiolite zircons used to interpret processes occurring at ancient mid-ocean ridges (MORs).

This contribution provides a detailed evaluation of textural features and chemical compositions characteristic of young (Neogene and Quaternary) zircons in ocean crustal rocks sampled on the flanks of modern MORs. A wide spectrum of geochemical data is presented, building on the previous study of ocean crustal zircon geochemistry (Grimes et al. 2007), and new analyses of zircon are presented that support geochemical distinctions between ocean crustal and continental zircon. Geochemical data were collected at the U.S. Geological Survey (USGS)-Stanford Ion Microprobe Laboratory using the sensitive high-resolution ion microprobe-reverse geometry (SHRIMP-RG), which currently allows for high-precision measurement of more than 35 elements with spot sizes of ~15 microns. Elemental correlations with Ti are emphasized to evaluate trace element behavior (within the entire population of ocean crustal zircons, as well as individual samples) with differentiation and decreasing temperature of parental magmas, as reflected by the Ti-in-zircon thermometer (e.g., Ferry and Watson 2007). Ocean crustal zircon therefore also record information about the behavior of trace elements within MORB magmas during zircon formation, consequently serving as a probe into the late stage, near-solidus evolution of lower crustal MORB magmas and derivative fractionates.

Geologic setting and host rock types

This study incorporates zircon from 35 samples acquired by drilling, submersible, and dredge along the northern MAR (near the 15°20′N Fracture Zone (FZ), Kane FZ, and Atlantis FZ), and along the SWIR at ~57°E (Atlantis II FZ) (Fig. 1). Crustal ages of sampling locations range from 1 to 14 Ma based on seafloor magnetic anomalies (Fujiwara et al. 2003; Williams et al. 2006; Baines et al. 2008) and Pb/U zircon ages (John et al. 2004; Schwartz et al. 2005; Baines 2006;

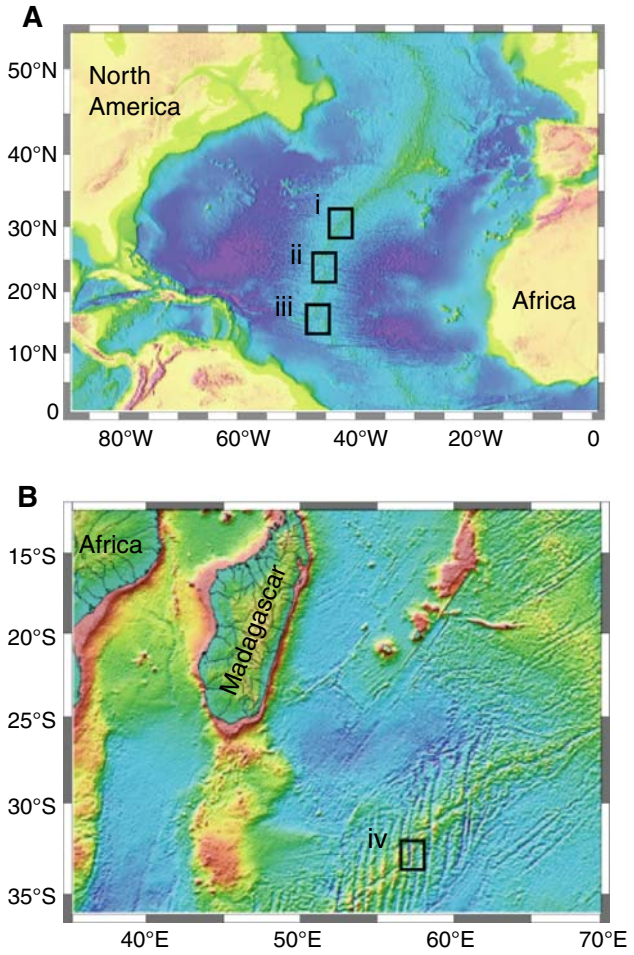

Fig. 1 Sampling locations. **a** Mid-Atlantic Ridge (MAR)—*i*. 15°20′ FZ-Ocean Drilling Program (ODP) Holes 1275D and 1270D; *ii*—Kane FZ-seafloor at Kane core complexes; *iii*—Atlantis FZ-Integrated Ocean Drilling Program (IODP) Holes U1309B and U1309D and seafloor at Atlantis Massif core complex. **b** Southwest Indian Ridge (SWIR) *iv*—Atlantis II FZ-ODP Hole 735B and 1105A, and seafloor at Atlantis Bank core complex. Basemap from Sandwell and Smith (1997)

Grimes et al. 2008; Cheadle et al. 2008). Rock types found to commonly host zircon include oceanic plagiogranite (i.e., anorthosite, diorite, tonalite-trondjhemite), and evolved Fe–Ti oxide ± amphibole gabbro (Fig. 2a–e). Zircon is also rarely found in less differentiated Fe–Ti oxide-poor gabbronorite and olivine gabbro. Common mineral assemblages for plagiogranite samples include plagioclase + amphibole ± quartz ± Fe-Ti oxides ± potassium feldspar ± titanite ± apatite, whereas gabbro samples comprise plagioclase + clinopyroxene + Fe–Ti oxide + apatite ± orthopyroxene ± amphibole ± titanite. The rock types represented by these samples are characteristic of evolved plutonic rocks in ocean crust. In this paper, gabbro samples containing >20% Fe–Ti oxides are referred to as Fe–Ti oxide gabbro, consistent with descriptions used by IODP Exp. 304/305 scientists (Blackman et al. 2006); samples with <2% Fe–Ti oxide are referred to as Fe–Ti oxide-poor gabbro (Table 1). Sample 3652-1333, described previously as a tremolite-chlorite schist (Grimes et al. 2007), is grouped here as Fe–Ti oxide gabbro, based on the presence of coarse-grained, relic Fe-oxides and abundant apatite.

Additional samples hosting zircon in this study comprise serpentinite and metamorphosed/deformed fault rocks with largely ultramafic protoliths (Table 1). The samples vary from fractured serpentinized harzburgite to talc-actinolite/tremolite-chlorite schist with relic chromite (Fig. 2), and are heavily altered (70–95%). Zircon recognized in thin sections of less-deformed samples is always localized in discrete millimeter to centimeter scale veins, or shear zones dominated by chlorite + actinolite/tremolite assemblages (e.g., Fig. 2f, h). Similar shear zones within serpentinite recovered in ODP Hole 1270D (Fig. 1) are interpreted to be altered plagiogranite melt impregnations, based partly on the presence of zircon (Jöns et al. 2009). We agree that the likely origin of zircon in the meta-ultramafic samples studied here is the intrusion of evolved melt prior to or during deformation, but the composition of melts intruding different samples may have been variable, and is difficult to determine given the high degree of alteration. These samples are therefore grouped together and referred to simply as 'veins in meta-ultramafic' samples.

Additional trace/accessory minerals observed in ocean crustal rocks include fluorapatite, chlorapatite, titanite, xenotime, monazite, and rutile, along with and trace metals (Au, Cu). Fluorapatite is a common accessory mineral in many igneous rocks, and is present in modal abundances up to 2% in Fe–Ti oxide-rich gabbro (e.g., Blackman et al. 2006). Monazite ((light REE)PO_4) and xenotime (YPO_4) are rare, but occur in all rock types including meta-ultramafic samples (Schroeder and John 2004).

Analytical methods

Electron microprobe

Quantitative and qualitative analysis of inclusions, and wavelength-dispersive (WD) X-ray mapping of zircon was performed using the JEOL JXA-8900R five-spectrometer electron microprobe located at the University of Wyoming. Quantitative analysis of major and minor elements in mineral and glass inclusions in zircon was conducted using a 15-kV accelerating voltage and 20 nA beam current. Natural minerals were used as standards, and the raw data was corrected using the standard ZAF correction. X-ray maps were acquired using a 15-kV accelerating voltage, 50 nA beam current, and 80 ms dwell time.

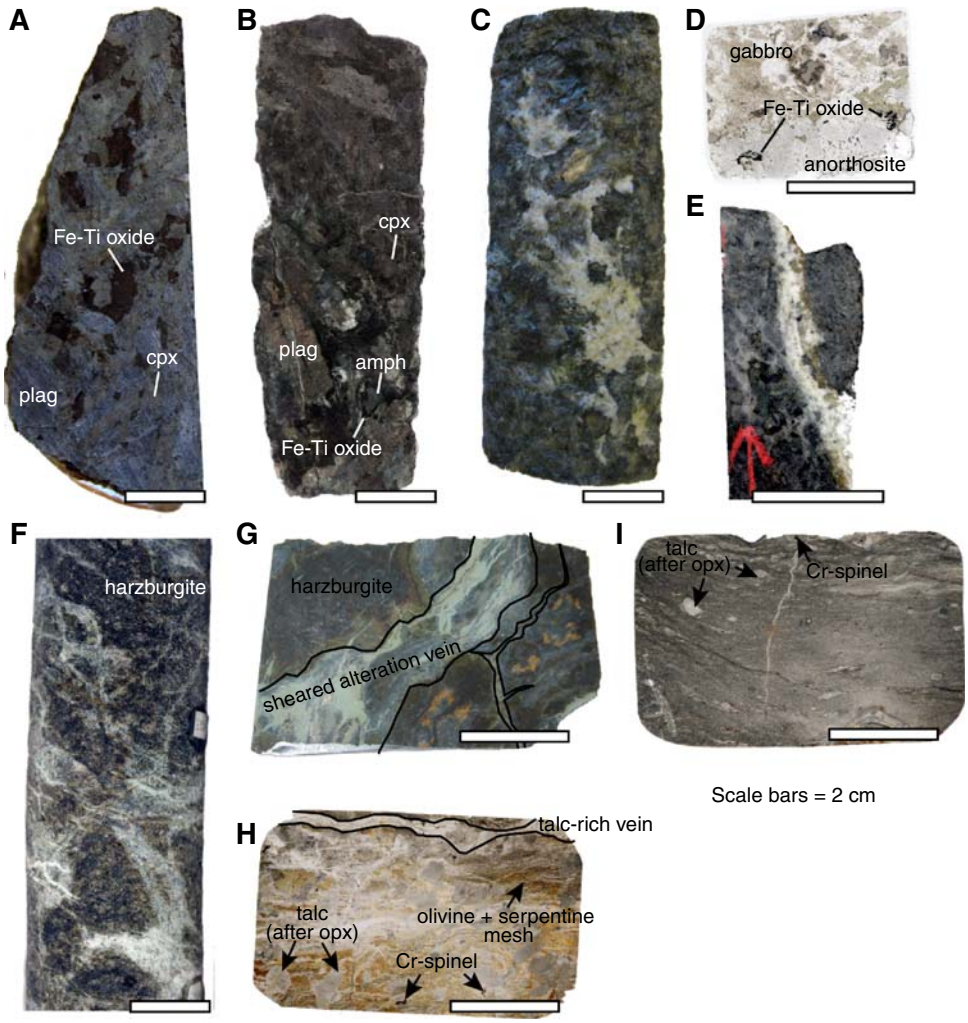

Fig. 2 Representative ocean crustal rocks host to zircon. **a** Fe–Ti oxide gabbro (U1309D-647). **b** Coarse-grained Fe–Ti oxide + amphibole gabbro (U1309D-355). **c** Plagiogranite (quartz diorite) dike intruding olivine-bearing gabbro (U1309D-1415). **d** Anorthosite dike intruding gabbro; zircon occurs in Fe–Ti oxide-rich clots (1105A-57). **e** Plagiogranite (trondjhemite) dike intruding gabbro (1275D-144). **f**, **g** Harzburgite with thin chlorite ± actinolite/tremolite shear zones; zircons occur only within the shear zones (1270D-19). **h** Serpentinized harzburgite (3646-1000); zircons occur at margin of talc vein and in chlorite ± actinolite/tremolite teration veins/fractures. **i** Talc-amphibole-chlorite schist with relic chromium spinel (3646-1205); 50–100 zircons occur in one (large format) thin section. *Plag* plagioclase, *cpx* clinopyroxene, *amph* amphibole

SHRIMP-RG

Trace element concentrations in zircon were measured during multiple sessions on the SHRIMP-RG located at the USGS-Stanford Ion Microprobe Laboratory between January, 2006 and January, 2009. Zircons were separated from whole rocks using standard crushing and mineral separation techniques, mounted in epoxy, polished, and imaged with reflected light and CL. Mineral separates from crushed sample volumes of 30–550 cm^3 yield 10 s to 1,000 s of zircons. Prior to SIMS analysis, samples were cleaned with a soapy solution, distilled water, EDTA solution, and again with distilled water before being dried and coated with 100 nm of Au. SIMS analyses were performed using a 3–6 nA primary beam current and 15–20 μm spot size.

Analyses dedicated to trace elements consisted of one block of two cycles. The consecutive cycles peak step sequentially from $^{9}Be^{+}$ to $^{254}UO^{+}$, and can be compared to check the reproducibility of raw counts during analysis of a single spot. Two concentration standards, including a primary standard (CZ3; a Sri Lankan megacryst, Ireland and Williams 2003), and a secondary standard (a gem quality crystal from Samé, Tanzania) were run after every ten unknowns. For quantification of titanium concentrations, these natural standards were repeatedly analyzed against synthetic Ti-bearing zircons that have been independently characterized by electron microprobe analyses. The isotopes $^{48}Ti^{+}$ and $^{49}Ti^{+}$ are measured for comparison; $^{48}Ti^{+}$ is subject to more critical secondary ion beam interferences from $^{96}Zr^{+}$ and $^{48}Ca^{+}$, but these potential interferences are limited by the high mass resolution ($M/\Delta M \approx 11{,}000$ at 10% peak height) of the SHRIMP-RG (Mazdab and Wooden 2006). Ti-in-zircon temperatures listed in Table 1 were calculated using the less abundant isotope, $^{49}Ti^{+}$, though concentrations determined from either isotope are in close agreement. Calcium, Al, and Fe were measured as tracers for identifying analyses where the ion beam may have unintentionally overlapped common inclusions. Chlorine and S are reported in Table 1 and the Supplementary Table as relative values (i.e., values of 1 indicate a concentration equivalent to the standard); the standards have not been calibrated for these elements and absolute

Table 1 Sample-averaged trace element analyses (SHRIMP-RG) of zircon from ocean crust

Rock type		Plagiogranite														
Sample[a]		U1309D-40			U1309D-215		U1309D-463	U1309D-570	U1309D-1040	U1309D-1415			1275D-10	U1309B-39		
Comment[b]		mag	por	l. rim	mag	por	mag	mag	mag	mag	por	l. rim	mag	mag	por	l. rim
S	rel.							1.0		1.3	37.8	1.1	1.5			
Cl	rel.							0.7		29.8	642.7	2.3	0.4			
F	ppm							17.9		16.5	24.8	14.4	15.5			
Al	ppm							24.7		23.5	270.2	11.9	25.2			
Ca	ppm	7.7	21.7	8.1	7.4	29.4	7.8	1.9		6.2	66.1	2.5	3.6	6.4	44.5	4.3
Fe	ppm	9.0	76.7	3.2	4.0	119.6	2.6	1.0		11.8	144.5	1.3	0.6	6.0	266.9	4.8
Sc	ppm							26.5		57.8	36.4	12.5	24.2			
Ti	ppm	8.9	8.0	2.3	7.5	11.5	11.6	14.1		15.6	54.1	2	20.9	9.9	13.1	3.4
P	ppm	3160	1051	1162	3471	8007	713	520		2222	1968	261	193	1646	1982	336
Y	ppm	16351	7980	3634	13986	32826	3724	3414		8966	6270	527	1258	5955	6839	1404
Nb	ppm							8.2		19.0	26.9	1.4	1.6			
La	ppm	0.12	3.41	0.12	0.80	20.10	0.02	0.09	0.07	0.27	2.92	0.02	0.04	0.04	11.96	0.02
Ce	ppm	160.3	141.7	23.4	115.4	270.4	14.7	154.9	230.8	261.1	102.0	3.9	3.8	44.2	66.5	16.9
Pr	ppm									0.38	0.65	0.04	0.10			
Nd	ppm	4.4	1.8	0.7	7.5	56.9	1.4	7.4	11.8	8.0	5.8	0.1	0.8	1.9	4.4	0.2
Sm	ppm	16.1	2.4	2.2	18.9	62.8	5.1	20.7	41.8	21.0	9.6	0.2	2.2	6.5	5.6	0.9
Eu	ppm	2.4	0.2	0.1	3.0	3.4	1.4	2.2	11.2	6.1	2.5	0.1	0.8	1.8	0.5	0.1
Gd	ppm	227	25	32	225	445	72	218	479	195	87	4	29	106	58	14
Tb	ppm									71	34	2	11			
Dy	ppm	1265	239	232	1082	1713	353	1123	2182	834	438	32	136	530	387	95
Ho	ppm									375	226	18	52			
Er	ppm	2773	1096	676	2205	3388	698	2221	3840	1576	1102	103	240	1090	1285	284
Tm	ppm									334	281	29	50			
Yb	ppm	5753	5285	2239	4733	9234	1164	4115	6672	2772	2756	313	395	1968	3820	761
Lu	ppm									457	531	74	72			
Hf	wt %	1.94	2.68	2.91	1.97	3.50	1.36	1.46	1.32	0.99	1.11	1.32	0.86	1.87	2.92	1.97
Th	ppm	328	816	26	159	572	37	356	245	1257	2967	68	11	347	570	171
U	ppm	515	1104	298	372	838	78	394	289	704	1771	145	22	272	1929	199
Temp (°C)[c]		733	720	625	719	755	753			786	905	624	817	744	768	654
Eu/Eu*[d]		0.10	0.07	0.03	0.14	0.07	0.25	0.17	0.25	0.30	0.28	0.37	0.31	0.19	0.09	0.11
Ce/Ce*[e]		226	174	74	76	10	58	137	182	276	23	42	21	130	20	146
# analyses		18	10	4	13	8	10	22	4	8	8	2	7	4	7	1

Table 1 continued

Rock type		Plagiogranite			Fe-Ti oxide gabbro											
Sample[a]		735B-26	735B-854	1105A-57	U1309D-355	U1309D-386	U1309D-564	U1309D-647		U1309D-820	U1309D-923		U1309D-1175		U1309D-1327	Kn180-2 9-1
Comment[b]		mag	mag	mag	mag	mag	mag	mag	por	mag	mag	por	mag	por	mag	mag
S	rel.							1.8	11.7							0.4
Cl	rel.							19.5	605.0							0.0
F	ppm							43.6	27.3							8.3
Al	ppm							22.6	229.7							10.3
Ca	ppm							5.1	43.3							0.8
Fe	ppm							8.3	672.7							0.4
Sc	ppm							43.4	18.2							44.2
Ti	ppm							6.6	31.8							18.2
P	ppm							6942	2181							504
Y	ppm							24459	9944							2164
Nb	ppm							4.7	2.5							0.8
La	ppm	0.05	0.07	0.04	0.05	0.04	0.04	0.08	1.71	0.06	0.20	1.50	0.20	0.75	0.23	0.01
Ce	ppm	29.8	93.2	23.2	38.2	110.1	16.5	123.7	48.7	50.3	455.0	68.3	263.5	11.0	33.6	10.4
Pr	ppm							0.29	0.56							0.17
Nd	ppm	1.8	5.2	2.2	3.6	5.9	2.3	7.5	5.8	5.3	13.7	2.9	11.9	1.2	7.7	1.3
Sm	ppm	5.5	12.4	7.4	11.8	20.8	6.4	31.0	10.4	17.3	33.0	6.6	34.2	2.0	15.7	3.9
Eu	ppm	2.1	3.0	1.4	1.3	4.8	1.7	1.2	2.0	4.4	6.1	1.4	5.6	0.5	2.5	1.3
Gd	ppm	59	121	80	135	251	73	403	103	199	333	77	364	23	139	44
Tb	ppm							163	43							17
Dy	ppm	242	548	361	652	1197	345	1998	601	867	1568	460	1468	153	599	207
Ho	ppm							840	334							85
Er	ppm	431	1169	682	1256	2153	655	3671	1685	1373	3270	1254	2520	531	984	395
Tm	ppm							749	408							93
Yb	ppm	723	2343	1171	2038	3459	1075	5713	3487	1956	6445	3000	3994	1444	1460	701
Lu	ppm							850	591							127
Hf	wt %	0.91	1.33	1.19	1.61	1.39	1.17	1.49	1.50	1.18	1.31	1.15	1.24	0.56	1.07	1.13
Th	ppm	46	138	37	155	186	180	2071	4148	661	1334	1193	706	331	118	233
U	ppm	40	186	83	275	232	186	2240	2688	406	1110	1291	329	550	247	323
Temp (°C)[c]								707	851							799
Eu/Eu*[d]		0.39	0.25	0.21	0.13	0.20	0.24	0.05	0.23	0.22	0.18	0.23	0.15	0.24	0.24	0.31
Ce/Ce*[e]		39	131	48	68	138	47	260	13	82	182	18	146	6	46	131
# analyses		10	10	12	5	5	6	5	7	9	6	3	14	1	9	11

Table 1 continued

Rock type		Fe-Ti oxide gabbro				Fe-Ti oxide-poor gabbro					veins in meta-ultramafic rocks						
Sample[a]		Kn180-2 117-27	Kn180-2 25-20	3652-1333		U1309D-588		JR31 12-68	JR31 22-1	Kn180-2 11-1	3646-1205	D3-21	3647-1359	3646-1000	1270D-19	1270D-25	Kn180-2 112-93
Comment[b]		mag	mag	mag	por	mag	por	mag	mag	mag	mag	mag	mag	mag	mag	mag	mag
S	rel.	0.4	0.3	1.0	4.2	1.2	8.4			0.5	1.2	1.2	1.3	0.9	0.9	1.2	0.7
Cl	rel.	0.0	0.0	4.2	33.0	1.2	167.1			0.0	0.7	0.7	0.6	0.4	0.7	0.7	1.0
F	ppm	6.8	7.9	45.0	36.7	14.2	29.5			11.0	15.7	14.0	15.7	12.9	11.3	11.2	27.2
Al	ppm	11.1	78.8	23.9	2774.7	25.1	234.9			34.9	137.8	67.5	85.1	18.4	22.7	26.0	10.8
Ca	ppm	0.9	4.9	5.1	34.0	2.4	254.6			1.2	6.1	5.5	4.1	3.3	4.1	4.0	2.0
Fe	ppm	6.1	1.8	4.2	1931.6	0.8	32.5			1.3	1.1	8.0	0.9	0.5	0.6	0.6	0.5
Sc	ppm	29.9	25.9	45.2	24.2	21.7	15.0			40.3	13.8	20.4	41.4	14.7	19.9	23.3	14.6
Ti	ppm	15.0	46.7	15.1	12.7	12.3	27.6	17.6	74.8	9.8	27.3	32.2	24.9	26.8	21.3	25.2	17.5
P	ppm	736	354	2221	966	994	2149	275	304	798	564	568	914	396	274	210	1101
Y	ppm	2303	884	15785	5936	5042	13461	1699	773	2946	2227	2679	6115	1589	1379	1209	2833
Nb	ppm	1.2	0.5	55.3	12.8	9.6	8.2			6.0	3.1	3.1	14.9	2.2	7.8	3.2	2.5
La	ppm	0.11	0.02	0.06	1.10	0.01	3.22	0.01	0.01	0.07	0.14	0.07	0.04	0.02	0.02	0.02	0.01
Ce	ppm	19.9	2.6	181.9	57.7	28.0	47.7	7.5	2.8	31.5	13.8	9.5	27.8	6.7	11.2	7.4	16.4
Pr	ppm	0.15	0.10	0.14	0.11	0.09	1.16			0.31	0.11	0.13	0.17	0.09	0.05	0.05	0.10
Nd	ppm	1.2	0.6	7.3	3.2	1.8	38.2	0.3	0.5	3.6	1.2	1.8	3.1	0.7	1.1	1.0	1.7
Sm	ppm	3.7	1.8	24.5	8.6	6.3	53.9	1.6	1.5	7.1	3.2	5.2	10.7	2.1	2.5	2.5	5.6
Eu	ppm	1.1	0.6	3.6	1.4	1.3	41.3	0.9	0.3	1.7	1.2	1.4	3.1	0.7	1.2	1.3	2.2
Gd	ppm	42	19	328	108	85	308	36	16	61	40	63	141	27	28	26	56
Tb	ppm	16	7	130	45	35	94	14	6	22	16	24	55	11	11	10	21
Dy	ppm	200	84	1603	570	465	1064	177	81	259	217	290	690	152	133	120	252
Ho	ppm	89	34	629	236	195	474	67	34	110	89	110	266	63	55	48	102
Er	ppm	421	152	2686	1060	899	2136	270	152	522	425	477	1132	306	261	217	458
Tm	ppm	99	36	526	219	191	529	58	35	122	91	96	228	69	58	46	94
Yb	ppm	799	259	3694	1636	1458	4828	453	290	1031	727	696	1681	557	463	361	744
Lu	ppm	148	47	563	272	246	931	80	54	190	135	123	290	106	91	68	126
Hf	wt %	1.35	1.02	1.32	1.08	1.36	2.58	0.80	1.19	1.55	1.16	1.18	1.22	1.12	0.96	0.78	0.73
Th	ppm	183	10	842	423	83	2833	60	11	224	20	17	400	8	33	14	5
U	ppm	260	10	655	426	180	4803	106	31	393	40	28	255	20	65	21	11
Temp (°C)[c]		780	914	773	767	765	851	799	976	737	848	865	829	847	820	840	787
Eu/Eu*[d]		0.27	0.34	0.12	0.14	0.23	0.97	0.57	0.21	0.28	0.33	0.29	0.30	0.31	0.41	0.48	0.38
Ce/Ce*[e]		232	44	452	53	126	6	68	33	200	57	29	77	41	92	57	121
# analyses		9	14	7	2	13	1	3	4	18	5	6	6	8	5	7	10

[a] Detailed sample information is given in the Supplemental Data Table

[b] mag = normal magmatic grains; por = porous domains; l. rims = luminescent CL rim overgrowths

[c] Uncorrected Ti-in-zircon temperature calculated using the equation of Ferry and Watson (2007)

[d] Eu-anomaly calculated using chondrite-normalized values (indicated by subscript $_N$): $Eu/Eu^* = Eu_N/[\sqrt{(Gd_N*Sm_N)}]$

[e] Ce-anomaly calculated using chondrite-normalized values: $Ce/Ce^* = Ce_N/[\sqrt{(La_N*Pr_N)}]$ or $Ce_N/[\sqrt{(La_N*(1/3) + Nd_N*(2/3))}]$ (See Supplemental Data Table for full details)

concentrations are therefore unknown. However, the relative values still allow an assessment of variations in abundance of these elements. Chlorine and S are almost certainly not structural constituents in zircon, and highly elevated values reflect overlap with fluid inclusions or daughter salt residues. The analytical run table for grains analyzed in January, 2006 included fewer elements but followed the same procedures. Selected geochemical analysis including only Hf, U, Th, and REE are also listed in Table 1 and Supplementary Table; these data were collected in conjunction with SHRIMP-RG Pb/U isotopic age analyses.

Element/^{30}Si ratios are derived from the time-averaged counts for each mass for both the standards and unknowns, and values for unknowns are then compared to those of the primary standard to determine concentrations. The secondary standard provides an independent check of data quality. For P, Sc, Ti, and Y, 1σ precision is <3%; for the measured REE (excluding La), Hf, Th, and U, 1σ precision ranges from 4 to 9%; the precision for La is $\sim$15%.

Morphology of zircon from ocean crust

Three types of zircon recovered from oceanic crust are defined based on morphology, cathodoluminescence (CL) imaging, and textural relationships observed in thin section. Grains interpreted as magmatic in origin (Types 1 and 2) are by far the most common (>95%), and resemble young igneous zircon typical of other geologic settings. The third type is recognized as having distinctive porosity, and coloration. Although relatively less abundant ($\ll$5% of all grains observed), Type 3 grains are fairly common and occur in $\sim$25% of the samples evaluated. These grains may reflect either alteration of primary magmatic zircon, extremely late crystallization within volatile-rich magma or both.

Textural types

Zircon grains most frequently recovered from oceanic crust are euhedral, doubly-terminated crystals that are colorless and transparent in transmitted light (Fig. 3a). These grains, Type 1, occur in all rock types, though they are characteristic of oceanic plagiogranite. Grain sizes between 50 and 250 μm in the long dimension and aspect ratios (length to width) of 1:1 to 5:1 are typical, but grains <5 μm to >1 mm long are observed. Though rare, aspect ratios up to 12:1 are noted for zircon from several plagiogranite samples from ODP Hole 1275D (Fig. 1); such zircons are characteristic of volcanic rocks, and may indicate rapid growth due to fast cooling and/or over-saturation (Hoskin and Schaltegger 2003). In thin section, Type 1 zircons often exist as inclusions in zoned, magmatic plagioclase and hornblende (Fig. 3a).

Type 2 grains are distinguished as having subhedral to anhedral crystal habit (Fig. 3b), but like Type 1 zircons, they are colorless and transparent in transmitted light. Grains defined as Type 2 have been identified in thin sections from both plagiogranite and gabbroic rock types, but are most commonly recovered from gabbro. Anhedral and fragmental zircon grains are also reported from gabbroic rocks in continental environments (e.g., Corfu et al. 2003), and this morphology has been suggested to result from late crystallization in interstitial melt pockets (Scoates and Chamberlain 1995).

Type 3 zircon grains are readily identified in mineral separates and in thin section by faint coloration (cloudy white, pink, yellow) and translucent to opaque optical properties under transmitted light. Polished thin sections and grain mounts show that this opacity is often due to a high density of micron-scale pores (Fig. 3c), or less commonly, numerous inclusions. Type 3 grains are often euhedral and faceted, and exhibit a similar range in size and aspect ratio as Type 1 grains. In thin section, irregular growth habits such as anhedral protrusions (Fig. 3c-i, iii) and linear trails of small (<10 micron) zircon crystals (Figs. 3c, 4a, b) can be associated with Type 3 grains. Characteristic micro-porosity is also observed within some euhedral apatite grains (Fig. 3c-ii, 4a). In both zircon and apatite, the micro-porosity can be well-developed across the entire grain, dispersed as discrete domains, or isolated at grain rims (Figs. 3c, 4a). Type 3 grains are mostly found in plagiogranite and evolved Fe–Ti oxide gabbro, and importantly we note that samples with Type 3 grains always contain Type 1 and/or 2 grains as well.

A sub-type of zircon occurs as smooth overgrowth rims that are conspicuously inclusion-free and luminescent in CL (Fig. 3c-vi, vii). The most prominent luminescent rims (up to 25 microns thick) occur on Type 3 grains, but they have also been observed as very thin (1–3 micron) rims on all textural types.

Internal features

Internal zonation was evaluated with CL imaging and wavelength dispersive electron microprobe X-ray mapping. In CL, normal magmatic grains typically show oscillatory (growth) and/or sector zoning, though they may also be flat and lack obvious zonation (Fig. 3a). Fine-scale growth zoning and homogenous internal structure are very typical of zircon from plagiogranite. Black/dark edges in CL are also occasionally observed (Fig. 3c-iv). Sector zoning is characteristically well-developed in zircon from gabbro, though a combination of sector and growth zoning is typical (Fig. 3b). Luminescent rims may be concordant or

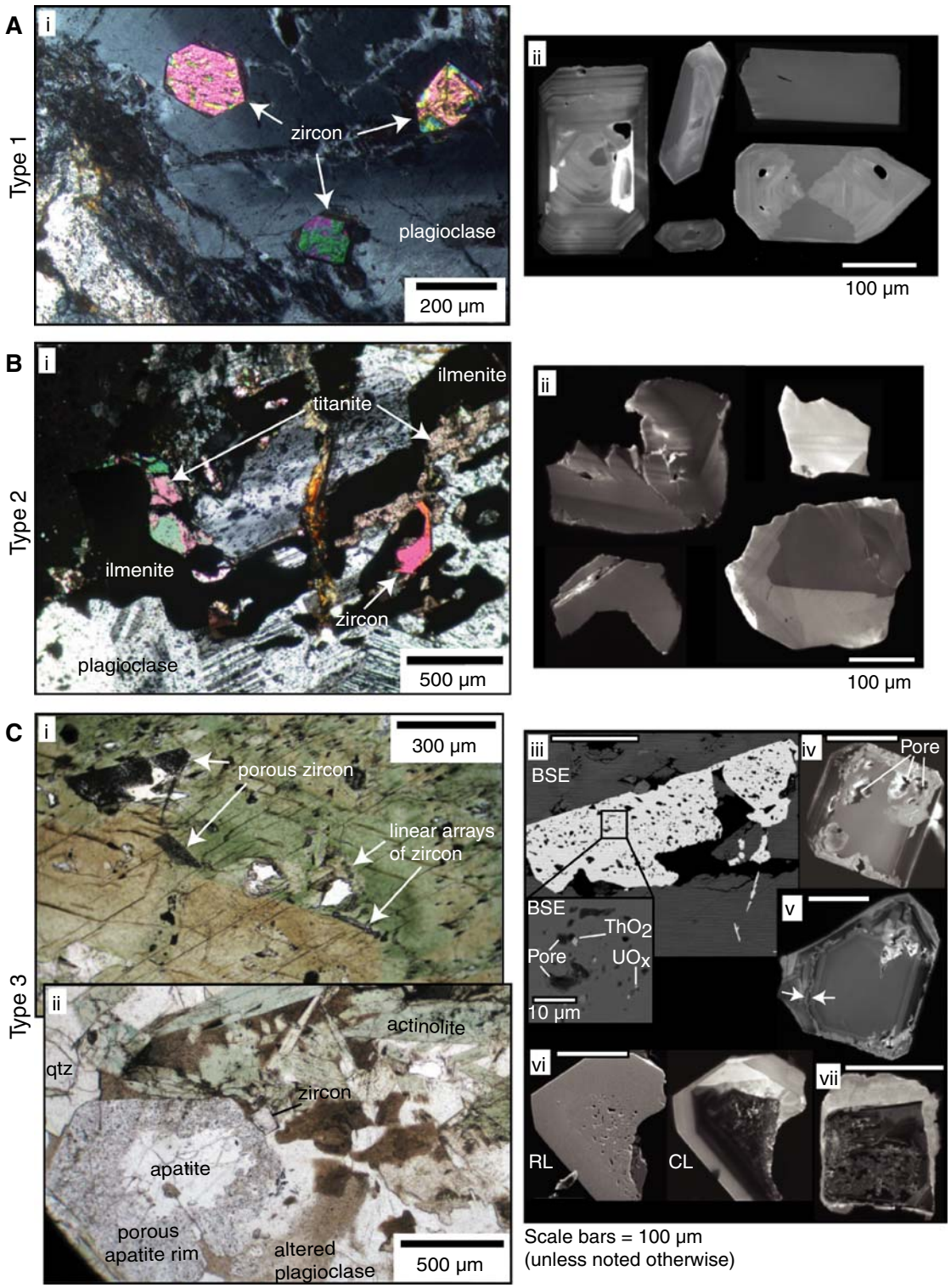

Fig. 3 Photomicrographs and SEM images of representative zircon textures and morphologies. **a** Type 1, euhedral zircons: *i*—inclusions in magmatically zoned plagioclase; *ii*—typical zoning patterns (all images CL). **b** Type 2, subhedral and anhedral magmatic zircon: *i*—late-stage crystals in evolved melt pockets (1105A-57); *ii*—anhedral grains recovered in mineral separates (all images CL). **c** Type 3, porous zircon: *i*—located along the boundary between brown and green amphibole (1309D-1415); *ii*—adjacent to large euhedral apatite with porous rim (1309D-1415); *iii*—backscattered electron (*BSE*) image of zircon in Ci; *iv, v*—euhedral, growth zoned zircons with incipient formation of irregular zonation and associated porosity; *v*—incipient alteration of magmatic zircon focused at the grain edge and along a narrow, dark CL band (indicated by *arrows*); *vi*—Subhedral grain with porous core and an inclusion-free, luminescent rim; *vii*—chaotically zoned, porous interior enclosed by luminescent rim. All images CL unless noted: *RL* reflected light

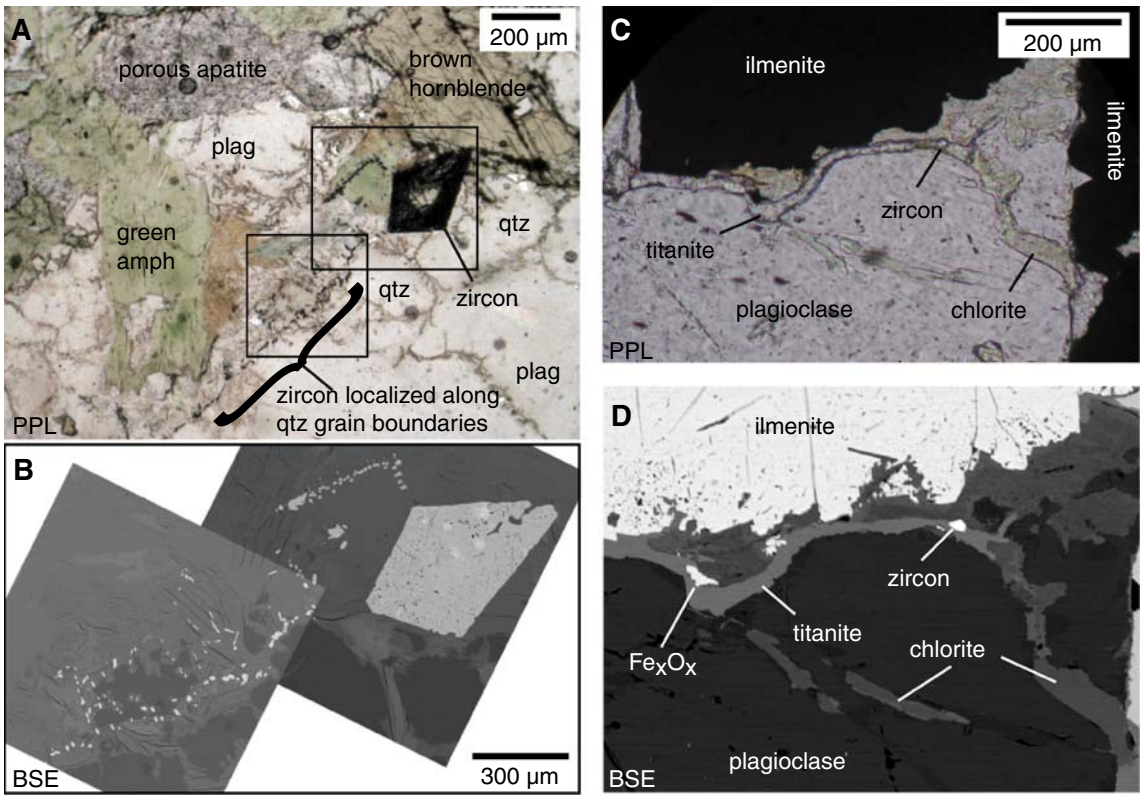

Fig. 4 Additional zircon textural relationships in host sample U1309D-1415. **a** Photomicrograph (*plane light*): trail of small zircon (typically <10 µm) in linear arrays (along former grain boundaries?) adjacent to a large euhedral zircon with a porous rim and non-porous core (see also Fig. 5c); *plag* plagioclase, *qtz* quartz, *amph* amphibole. **b** BSE image of area outlined in **a**—the bright grains are zircon; **c** Hydrothermal vein comprised primarily of titanite and chlorite hosting a single zircon grain; vein material formed from Ti and Fe derived from the adjacent ilmenite, and Ca, Al, and Si from the host plagioclase. **d** BSE image of **c**

discordant to zonation in the interior of the grain, and usually exhibit faint growth zoning.

Although qualitative in nature, X-ray mapping indicates zoning of specific elements, and often show enrichment in Hf toward grain edges. Yttrium and P are strongly coupled and exhibit well-developed oscillatory zonation (Fig. 5).

The morphology and internal zonation observed for Type 1 and 2 grains are similar to magmatic zircon from continental rocks (e.g., Hanchar and Miller 1993; Rubatto and Gebauer 2000; Corfu et al. 2003). These observations, as well as geochemical features discussed in following sections, indicate that Type 1 and 2 grains in ocean crustal rocks are magmatic in origin. Geochemical distinctions between these types have not been identified, and so they are henceforth referred to collectively as 'normal magmatic grains'. In contrast to normal magmatic grains, zonation within Type 3 zircon is often perturbed, convoluted, or chaotic (Fig. 3c). In some instances, perturbed zonation and micro-porosity coincide with specific growth zones within euhedral, otherwise oscillatory zoned zircons (e.g., Fig. 3c-iv & v), giving the impression that the porosity results from alteration of preexisting magmatic grains.

Inclusions

Primary inclusions hosted by zircon from oceanic crust provide information on the additional phases co-crystallizing during zircon formation. The two varieties of inclusions observed include (1) mono-phase mineral inclusions, and (2) irregularly shaped multiphase inclusions (glass + vapor bubble) likely indicative of melt trapped during zircon crystallization (Fig. 6). Inclusions are abundant in zircon from plagiogranite, and commonly comprise fluorapatite, sodic plagioclase, quartz, orthoclase, hornblende, and glass inclusions. Less common inclusions in plagiogranite-hosted zircons include chlorapatite, titanite, xenotime, monazite, sulfide, ilmenite, and rutile. Representative electron microprobe analysis of high-Si inclusions are given in Table 2, and show that these glass inclusions may contain 76–83 wt% SiO_2. Inclusions are less abundant in zircon from gabbroic rocks, but fluorapatite, sodic plagioclase, hornblende, ilmenite, and quartz have been identified. Zircon from veins in meta-ultramafic samples contain both inclusion types, which taken with the presence of sodic plagioclase, quartz, glass inclusions, and

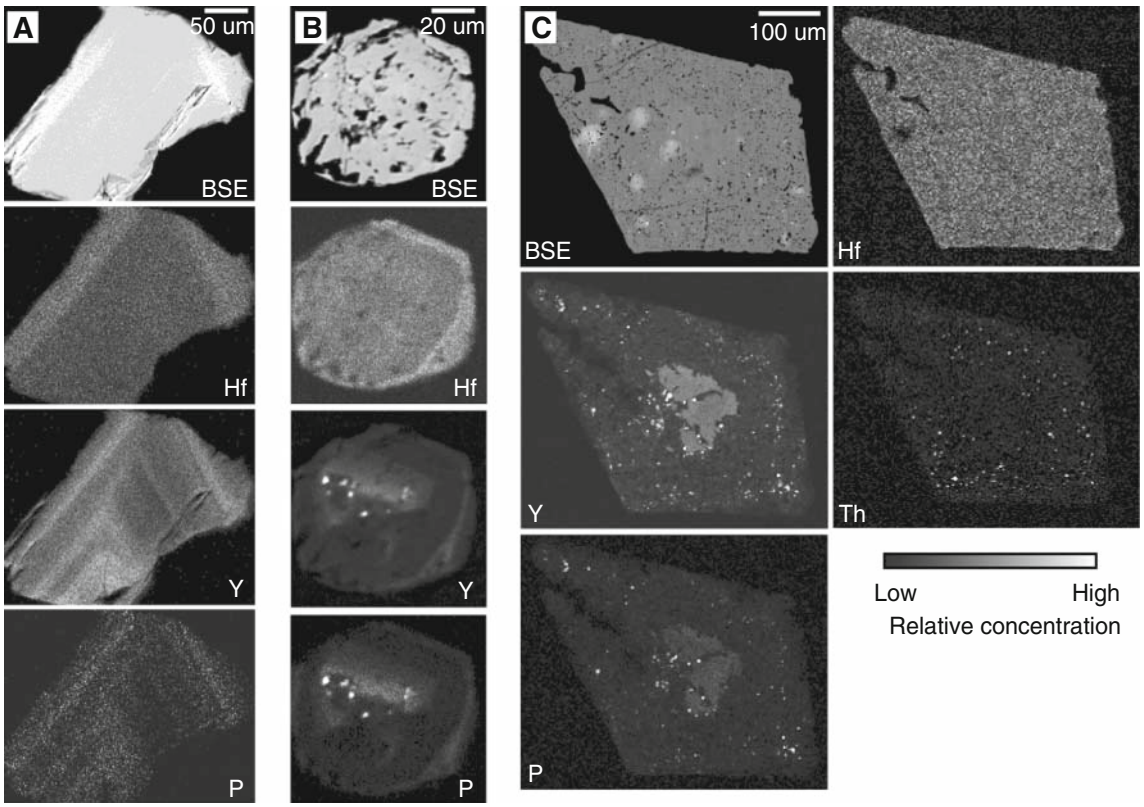

Fig. 5 X-ray (WD) maps showing compositional zoning in zircon. **a** Growth zoning characteristic of Type 1 and 2 grains; Hf becomes enriched at the rim, whereas Y and P exhibit oscillatory zoning. **b** Porous zircon with a xenocrystic core enriched in yttrium and phosphorus; Hf-enrichment also occurs at the rim; **c** Large euhedral zircon (see Fig. 4a) with highly porous rim, and a relatively non-porous core. The core exhibits generally uniform concentrations of Y, P, and Th. In contrast, the porous rim contains micron-scale inclusions of xenotime and ThO_2

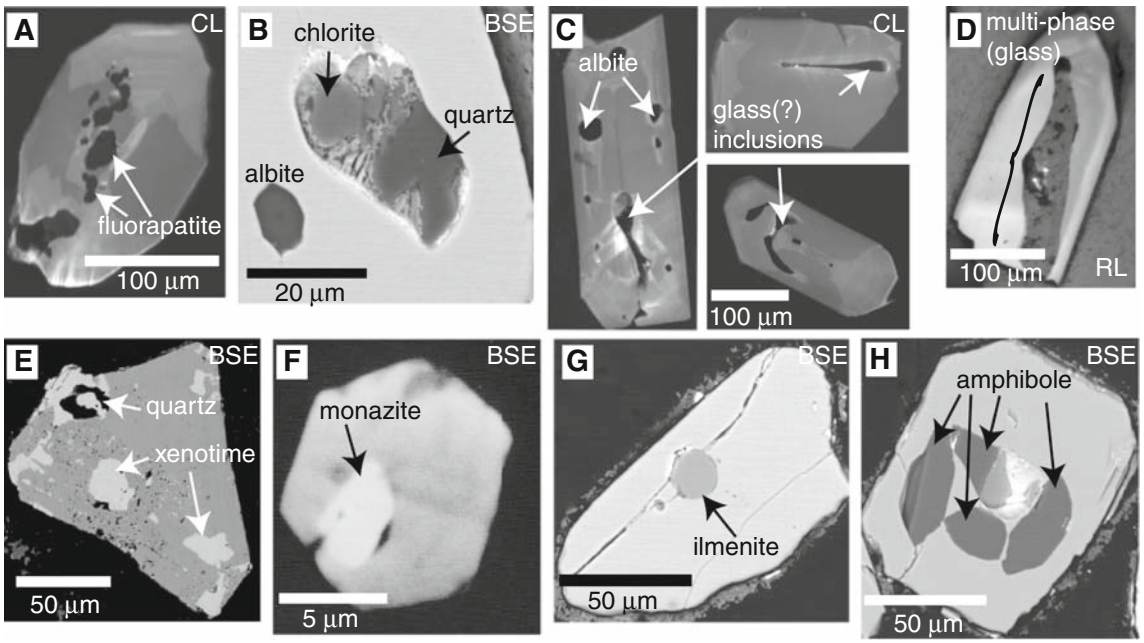

Fig. 6 Common inclusions in ocean crustal zircon. The multiphase inclusion shown in **d** likely represents devitrified glass; irregular boundaries defined by subtle brightness contrasts in BSE separate quartz, orthoclase, and albite within this inclusion (1275D-171, Table 2)

Table 2 Representative electron microprobe analyses of Si-rich inclusions in zircon from ocean crust

wt. %	3646-1205_i1	3646-1205_i2	3646-1205_i3	D588_i2	75D10_i2	75D171_i1.1	75D171_i1.2	75D171_i1.3	75D200_i3
SiO_2	67.3	95.8	83.3	76.1	76.1	67.9	66.1	97.5	78.8
TiO_2	–	–	–	–	0.02	–	–	0.04	–
Al_2O_3	20.4	1.8	10.0	13.7	15.9	20.4	18.5	0.25	12.9
FeO	0.05	0.02	0.00	0.03	0.01	0.02	0.05	0.03	0.02
MgO	0.02	–	–	–	–	–	–	–	–
CaO	1.01	0.09	0.50	1.03	1.03	0.68	0.25	0.01	0.5
Na_2O	10.7	0.8	5.8	2.7	3.6	10.0	3.4	0.1	7.2
K_2O	0.25	0.0	0.0	0.8	2.3	1.4	9.7	0.0	0.2
Total	99.8	98.6	99.6	94.4	98.9	100.5	98.0	97.9	99.7
XAn (mol %)	4.9					3.6	4.0		
Phase	Albite	Quartz	Glass?	Glass?	Glass?	Albite	K-feldspar	Quartz	Glass?

'–' below detection

Glass? indicates abundances do not indicate a stoichiometric mineral formula; inferred glass inclusion

monazite (e.g., Fig. 6b, d, f) supports an interpretation that these grains originated from evolved melt.

Type 3 zircon contain inclusions similar to those discussed above, and in addition may host sub-micron silicate, phosphate and oxide inclusions with U, Th, Y, or REE as the dominant cation based on WD X-ray maps (Fig. 5), and qualitative electron microprobe (EDS) analysis (Fig. 3c-iii inset). The distinctive micro-pores in these grains occur as <10 micron pits or cavities on grain surfaces (Fig. 3c-iii inset), and likely represent fluid or vapor inclusions exposed during polishing.

Zircon geochemistry

Geochemical character of ocean crust zircon

The following discussion is based on 356 analyses of zircon (267 grains) from 35 rock samples (Supplementary Table). Sample-averaged zircon geochemistry is given in Table 1. The ocean crustal zircon population shows a significant range in major, minor, and trace element concentrations comparable to the variability reported for zircon derived from rocks with a continental affinity. As in other terrestrial zircon populations, the most abundant elements measured include Hf, Y, P, heavy REE (HREE), U, and Th. Hafnium concentrations vary from 0.56 to 5.80 wt%. The measured concentrations of other elements range from 199 to 73,705 ppm Y, 131–17,414 ppm P, 3–5,544 ppm U, and 2–10,900 ppm Th. The greatest measured trace element abundances occur in the Type 3 zircon, though they likely reflect in part analysis of the micro-inclusions observed on backscattered electron images (Fig. 3c) and X-ray maps (Fig. 5). Excluding Type 3 zircon, the maximum concentrations observed are 3.73 wt% Hf, 4.08 wt% Y, 0.95 wt% P, 3,106 ppm U, and 7,556 ppm Th.

Geochemical variation diagrams for normal magmatic zircon from ocean crust are shown in Figs. 7 and 8, and representative suites of zircon from individual samples are shown in Fig. 9. Figure 10 compares normal magmatic zircons with Type 3 (porous) zircon. In Figs. 7, 8, and 10 analyses are grouped by host-rock type. Many of the trace/major element correlations discussed in the following sections are shown by zircons from plagiogranite and gabbro. Data from zircons hosted by veins in meta-ultramafic samples show either weak or no correlations, likely due to variability in the composition of melts crystallizing zircon in the meta-ultramafic samples. However, the original compositions of the vein are difficult to determine due to heavy alteration and deformation.

Textural Types 1 and 2: normal magmatic ocean crustal zircon

Correlations between Ti and various elements are shown in Fig. 7 to assess substituting-element behavior with Ti-in-zircon crystallization temperature (Watson and Harrison 2005; Watson et al. 2006; Ferry and Watson 2007). Normal magmatic ocean crustal zircons generally become enriched in Hf, U, Y, and total (Σ) REE with decreasing Ti (Fig. 7). These correlations are particularly well-defined by zircon from all rock types for tetravalent cations such as Hf and U, perhaps reflecting the fact that zircon is the main reservoir for these elements. Hafnium, the only element other than zirconium, silicon, and oxygen to consistently occur as a major element in zircon, generally increases in concentration from ~0.6 to 1.5–2 wt% as Ti concentrations decrease from 100 to <10 ppm (uncorrected temperatures of 1,020 to <750°C). An inflection in the trend occurs at

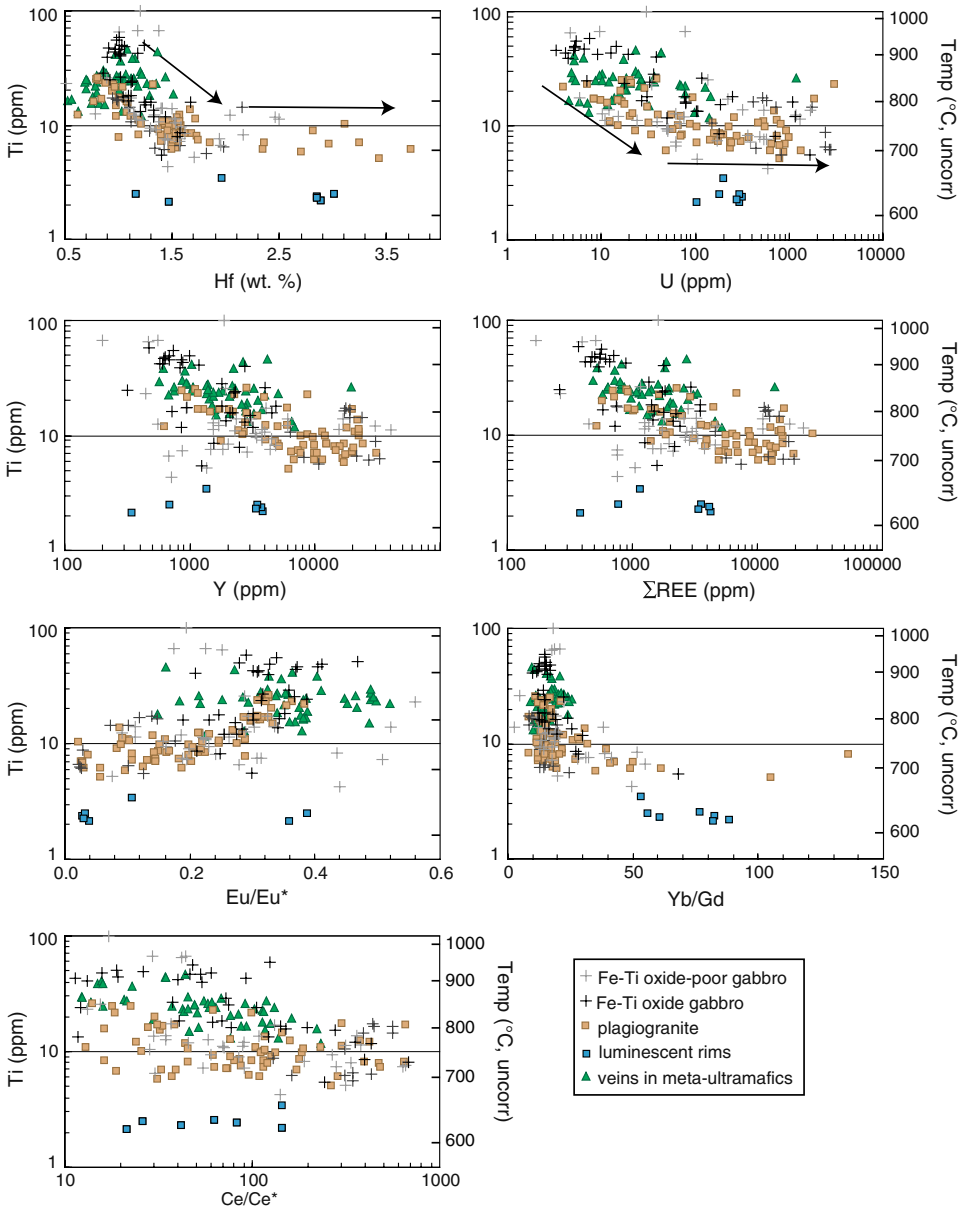

Fig. 7 Titanium plotted versus selected element concentrations and ratios for normal magmatic zircon (Types 1 and 2). *Scale on the left-hand side of each diagram* represents titanium concentration; *the right-hand scale* shows uncorrected Ti-in-zircon temperature, based on the recalibrated Ti-in-zircon thermometer of Ferry and Watson (2007). *Arrows* are shown on the upper two plots to emphasize the inflection in these trends as discussed in the text

1.5–2.0 wt% Hf, and further Hf-enrichment occurs at a relatively constant concentration of Ti. Suites of zircon from individual samples from the Spirit Mountain Batholith, a Miocene composite granitoid pluton system in southern Nevada, also exhibit this behavior (Claiborne et al. 2006). Uranium, Y, REE, Eu-anomaly (Eu/Eu*), and Yb/Gd ratios reveal a similar inflection when plotted against Ti (Fig. 7), though the trends are mostly defined by zircons from plagiogranite. These inflections define minimum Ti-in-zircon temperatures where progressive trace element enrichment occurs (Fig. 7), which may represent the eutectic temperature of the melt crystallizing zircon.

The observed Hf-enrichment with decreasing Ti concentration reflects progressive fractionation, and is consistent with previous studies that note higher Hf concentrations in zircon from more differentiated rocks (i.e., higher silica contents, decreasing Ti-in-zircon temperature) (e.g., Hoskin and Schaltegger 2003; Claiborne et al. 2006; Fu et al. 2008), as well as single grain X-ray maps that indicate enrichment of Hf towards zircon rims (Fig. 5). The behavior of Hf can be explained by zircon being the prime reservoir for both Zr and Hf, but preferentially incorporating Zr over Hf during crystallization. Zircon saturation therefore decreases the Zr/Hf ratio in the melt, which is then inherited by later formed grains (Claiborne et al. 2006; Wooden et al. 2006). The Ti-in-zircon temperature and Hf concentration therefore both serve as effective indicators of zircon fractionation, and, correspondingly, magma evolution. Hafnium may be a better index of fractionation than temperature for the most

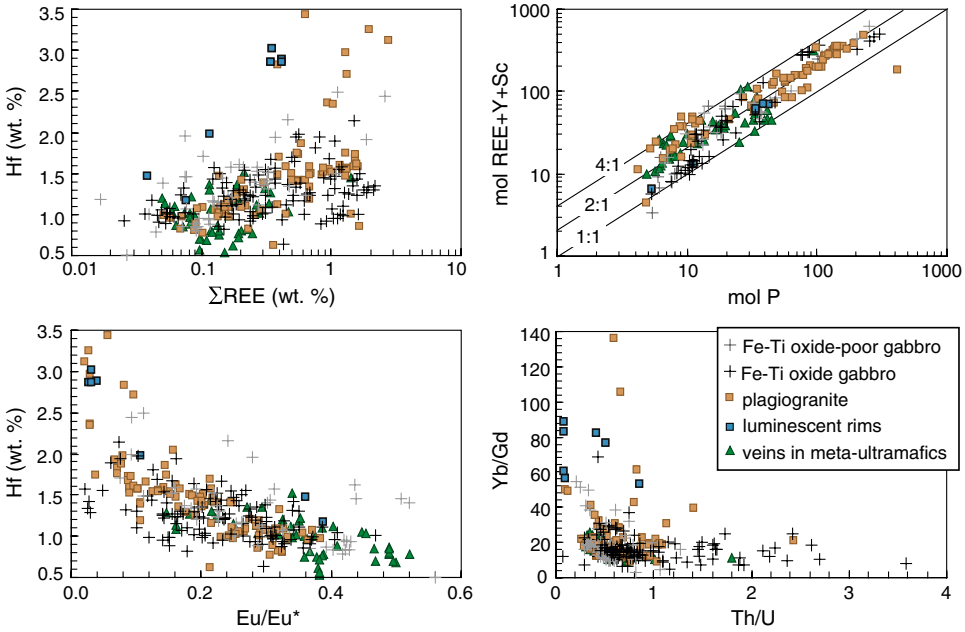

Fig. 8 Additional geochemical variation diagrams for normal magmatic zircon (Types 1 and 2). See text for details

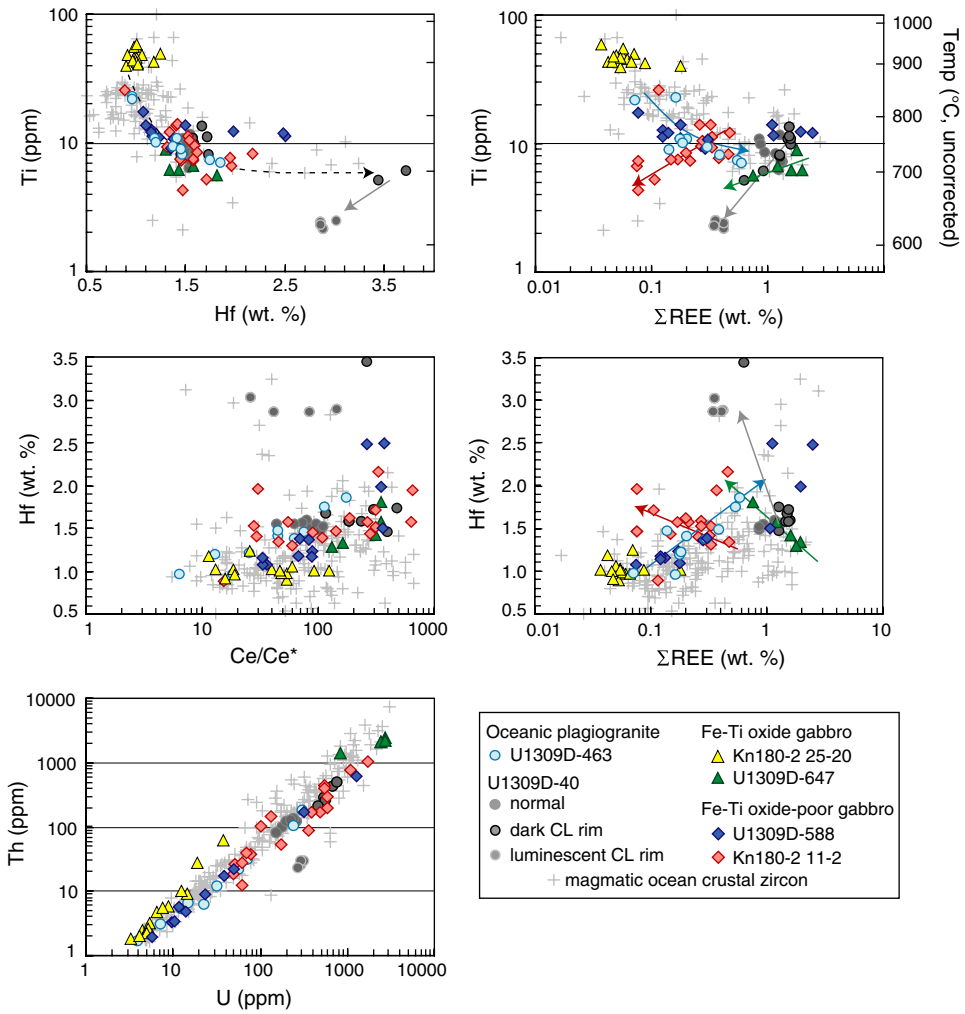

Fig. 9 Geochemical variation diagrams for suites of zircon from individual samples. *Right-hand scale on the top two plots* shows uncorrected Ti-in-zircon temperature. *Arrows* shown highlight trends discussed in the text. Note that different individual sample suites may exhibit opposite correlations

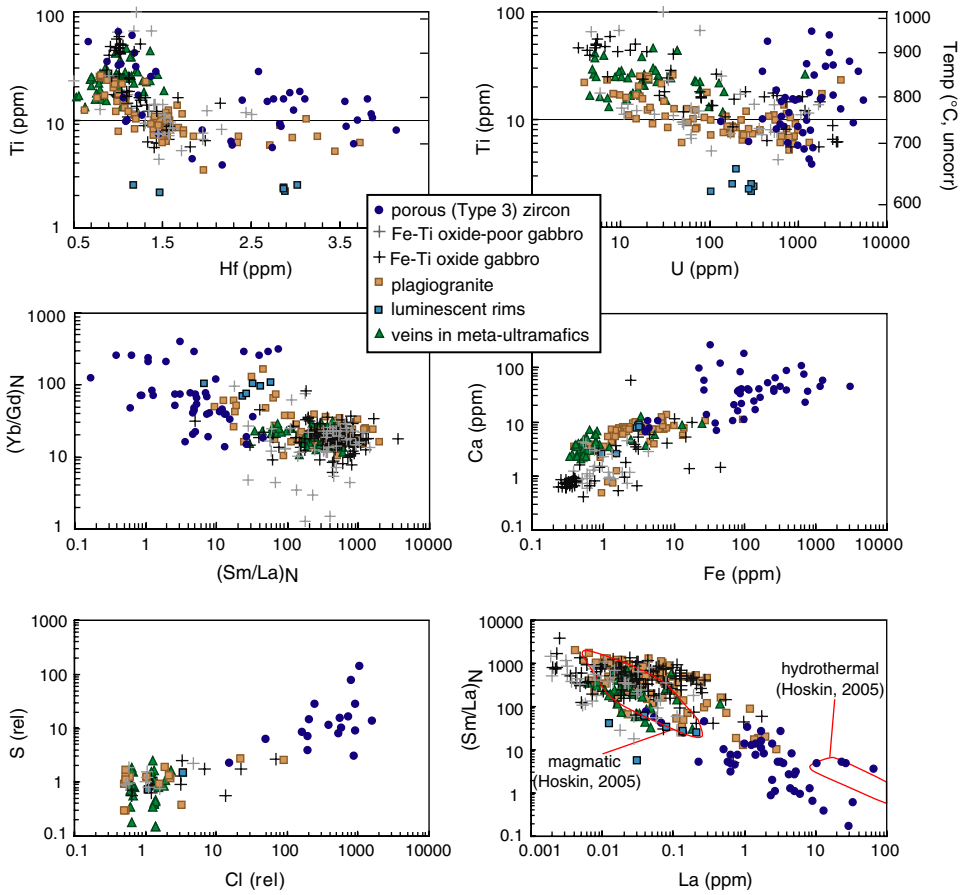

Fig. 10 Geochemical variation diagrams comparing Type 3 (porous) and normal magmatic (Types 1 and 2) ocean crustal zircon. *Right-hand scale on the top two plots* shows uncorrected Ti-in-zircon temperature. Fields shown on the plot of $(Sm/La)_N$ versus La were proposed by Hoskin (2005) for discriminating zircons that have magmatic and hydrothermal zircons

highly evolved zircons, for which Ti-concentration remains somewhat constant.

By comparison with Hf and U, correlations of ΣREE and Y with decreasing Ti-concentration are less well-defined, particularly for gabbro-hosted zircon. Scatter in these trends results because in some samples, ΣREE and Y (not shown) correlate positively rather than negatively with Ti (Fig. 9). For example, samples Kn180-2 11-1 and U1309D-647 show ΣREE enrichment with increasing Ti (and decreasing Hf). Some samples exhibit relatively little variation on these plots, and instead form a cluster of data points (e.g., Kn180-2 25-20) implying that zircon records little fractionation due to crystallization over a relatively small temperature range. Trends reported for continental granitoid zircon suites tend to show decreasing ΣREE abundance from early to late zircon growth (Wooden et al. 2006; Pettke et al. 2005), which contrasts with the relatively well-developed correlation defined by zircons from most oceanic plagiogranites. These contradictory correlations most likely reflect local differences in the relative timing of saturation between zircon and other accessory minerals (including apatite, titanite, xenotime, and monazite) that sequester REE. Apatite and titanite are quite common, particularly in Fe–Ti oxide gabbros where they may comprise up to 1–2 modal % of the rock (e.g., Dick et al. 2000; Blackman et al. 2006). The onset of crystallization of these minerals would lead to depletion of REE in the melt, resulting in lower REE concentrations in later-formed zircon. In contrast, if zircon is the primary REE-sequestering mineral crystallizing, REE may behave like Hf and build up in the melt as zircon initially takes up Zr preferentially. Since zircon is the primary reservoir for Hf, saturation of other accessory minerals will not significantly effect Hf concentration of the melt, possibly explaining why all individual samples show a consistent trend of Hf enrichment with decreasing Ti concentration (Fig. 9).

Other than Hf, the most abundant substituting elements in zircon are Y, P, and REE. The substitution of these cations in zircon requires a coupled substitution mechanism to achieve charge balance. A common substitution cited in the literature is the coupled xenotime-type ($(Y^{3+}$, REE^{3+}, $Sc^{3+}) + P^{5+} = Zr^{4+} + Si^{4+}$) (e.g., Speer 1982; Halden et al. 1993), resulting in the strongly linear co-variation of Y + REE + Sc and P (Fig. 8). The xenotime-type coupled substitution is also expressed by the correlation of Y and P in X-ray maps (Fig. 5). However, as in many natural zircon populations (Hoskin and Schaltegger 2003), zircon from ocean crust contain excess $(REE + Y + Sc)^{3+}$ relative to what is charge balanced by P. Molar $(REE + Y + Sc)^{3+}$:P^{5+} ratios are almost always

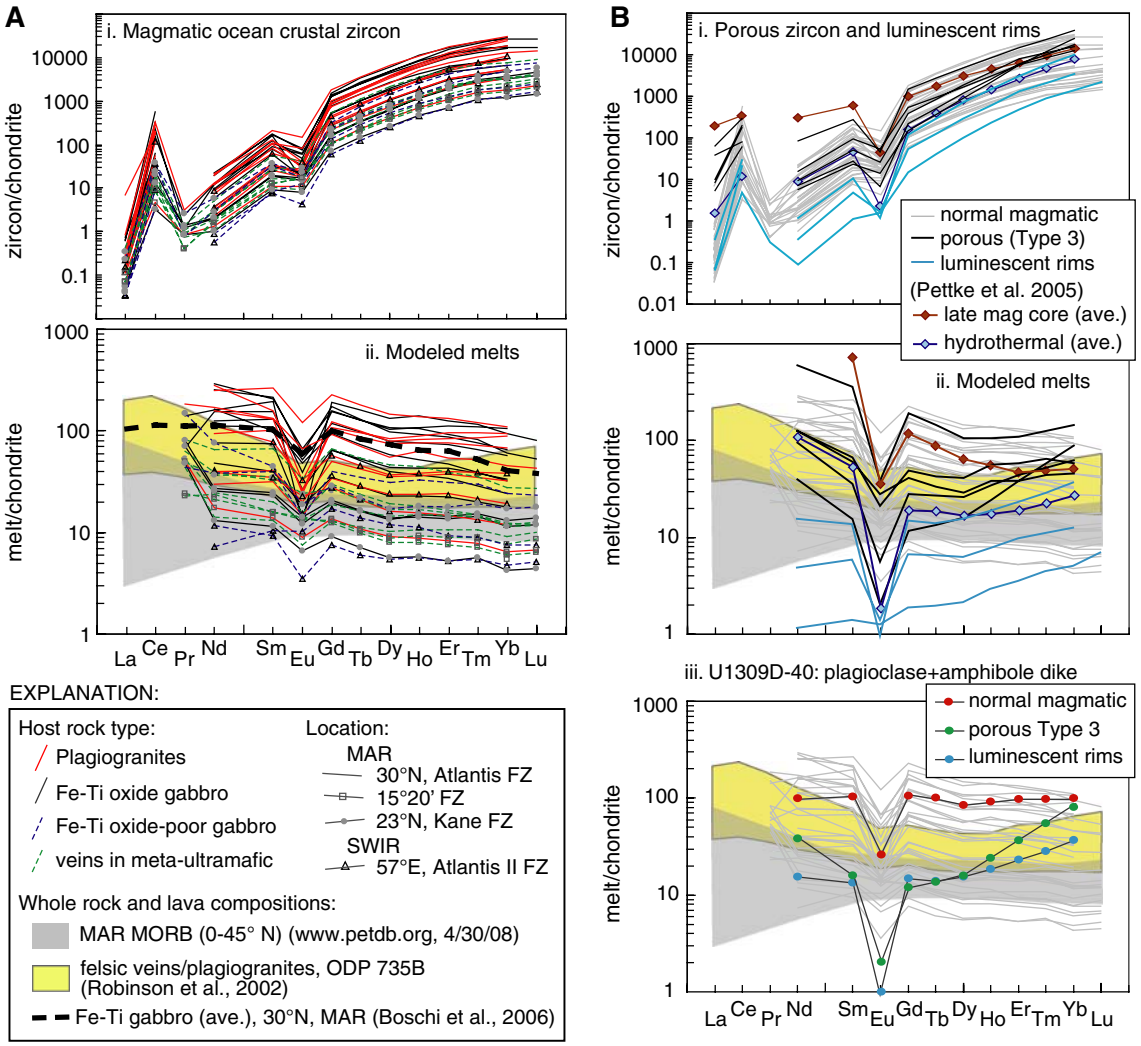

Fig. 11 Chondrite-normalized REE patterns and equilibrium melt modeling from sample-averaged data. **a** normal magmatic ocean crustal zircon—*i*. zircon REE patterns (Table 1); *ii*—melt REE patterns modeled from zircon compositions shown in **a***i*. **b** Type 3 (porous) zircons and luminescent rims—*i*. zircon REE patterns (Table 1); *ii*—melt REE patterns modeled from zircon compositions shown in **b***i*. Chondrite-normalized REE concentrations for late-magmatic and hydrothermal zircon from the Mole Granite, Australia (Pettke et al. 2005) are shown for comparison. Note the same concave-upward shape of the modeled melt REE patterns for the Mole Granite zircons, and Type 3 ocean crustal zircon, which is clearly distinct from normal magmatic zircon patterns. Chondrite-normalizing values are from Korotev (1996). Zircon-melt partition coefficients reported by Sano et al. (2002) were used for modeling. The field of ODP Hole 735B plagiogranites shown in **a** and **b** is defined by 12 bulk rock analyses reported by Robinson et al. (2002)

greater than 1:1 and are typically between 2:1 and 4:1 (Fig. 8), requiring additional substitutions to accommodate the excess trivalent cations that are presently unknown. Several substitutions, including the incorporation of divalent or trivalent species into interstitial sites or the incorporation of hydroxyl ions have been suggested to achieve this charge balance (review in Hoskin and Schaltegger 2003).

Chondrite-normalized REE patterns for magmatic ocean crustal zircon closely resemble patterns for magmatic zircon from continental crustal rocks (Hinton and Upton 1991; Hoskin and Ireland 2000; Hoskin and Schaltegger 2003), exhibiting smooth enrichment from the LREE toward the HREE apart from ubiquitous Eu- and Ce-anomalies (Fig. 11a-i). The pattern arises due to variable lanthanide REE compatibility in the ^{viii}Zr site due to lanthanide contraction. The ionic radii of REE decreases from La ($^{viii}La^{3+}$, IR = 1.16 Å) to Yb ($^{viii}Yb^{3+}$, IR = 0.985 Å) with the heavier REE's having radii closer to that of $^{viii}Zr^{4+}$ (IR = 0.84 Å), leading to preferential incorporation of the HREE. These crystal chemical effects result in REE patterns with very uniform shape and slope (Fig. 11a-i). On the other hand, ΣREE concentrations vary widely, and weakly correlate with rock type (Fig. 7). Zircons from Fe–Ti oxide-poor gabbro and veins in meta-ultramafic rocks generally have lower REE concentrations, and

plagiogranite and Fe–Ti oxide gabbro samples host zircons that are more enriched (Fig. 11a-i).

In addition to REE concentration, prominent differences are observed in the magnitude of the Eu- and Ce-anomalies. Negative Eu- and positive Ce-anomalies are pronounced in all ocean crustal zircons (Fig. 7, 11a-i). For zircons in plagiogranite and Fe–Ti oxide gabbro, the magnitude of the Eu-anomaly increases with increasing Hf and decreasing Ti concentrations (Figs. 7, 8, 9), suggesting that Eu gets depleted in the melt relative to adjacent REE (Sm, Gd) with fractionation. This observation is consistent with Eu^{2+} being partitioned by plagioclase, other feldspar, or titanite during fractional crystallization. The Ce-anomaly results from the presence of $^{viii}Ce^{4+}$ (IR = 0.97 Å), which is more compatible in zircon than trivalent $^{viii}Ce^{3+}$ (IR = 1.14 Å) due to its equivalent charge and closer ionic radius to $^{viii}Zr^{4+}$. The magnitude of the Ce-anomaly is therefore, in part, a function of the redox conditions of the melt/fluid from which zircon crystallized (e.g., Ballard et al. 2002). However, the anomaly may also be affected by partitioning of the $LREE^{3+}$ into other phases during fractional crystallization (Pettke et al. 2005). A combination of changing redox and partitioning into other phases probably contributes to the weak correlations observed between Ce-anomalies and Ti (Fig. 7) and Hf (Fig. 9), thus complicating any assessment of evolving redox conditions based on Ce-anomalies in zircon from these samples.

Textural Type 3: porous zircon

In addition to clear textural distinctions, the porous (Type 3) zircons have contrasting geochemical characteristics with normal magmatic grains (Fig. 10). In some cases mixed analysis of zircon and mineral inclusions (e.g., Fig. 3c-iii) or residues within the pores could contribute to these differences. In normal magmatic zircons, non-constituent elements such as Ca, Fe, and Al (analyzed primarily to screen for common inclusions) occur at concentration levels of <10 ppm Fe and Ca (Fig. 10) and <30 ppm Al (Table 1). However, they are consistently elevated by one to two orders-of-magnitude in porous domains (Fig. 10), indicating contamination from sources other than crystalline zircon. Moreover, measured Cl and S contents in Type 3 zircons are elevated up to 1,000 times those observed in normal magmatic grains (Fig. 10); these elements are almost certainly not structural constituents in zircon, and indicate that fluid inclusions or salt residues within the pores have been analyzed. Caution is thus required when evaluating analyses from porous zircons, but the observed geochemical trends still help to characterize these grains and provide clues about the conditions under which they formed.

Type 3 zircons often contain relatively high Hf and U concentrations; over half of the Type 3 grains analyzed (24 out of 47) contain >2 wt% Hf, whereas only about 7% of normal magmatic zircon contain more than 2 wt% Hf (Fig. 10). Elevated Hf suggests that the porous texture occurs in more differentiated zircons, however not all porous grains contain high Hf (Fig. 10). Uranium concentrations are consistently elevated in Type 3 zircon relative to normal magmatic grains. If the micro-porosity and inclusions are the result of alteration of normal magmatic grains, then perhaps the measured Hf concentrations (Hf being the most compatible substituting element in zircon) reflect the original trace element concentration of the unaltered grain better than other elements. Type 3 grains loosely adhere to the trend of increasing Hf with decreasing Ti observed for normal magmatic zircon, but U shows no correlation with Ti, and measured Ti concentrations are higher than expected based on trends defined by the population of normal magmatic zircons (Fig. 10). Due to contamination from residues in the pores (as indicated by elevated Fe, Ca, and Al), Ti concentrations measured on the porous grains are not considered to be representative of the concentration of Ti in crystalline zircon.

Additional geochemical properties that contrast normal magmatic and Type 3 zircon are chondrite-normalized $(Yb/Gd)_N$ and $(Sm/La)_N$ ratios (Fig. 10). Type 3 grains have an average $(Yb/Gd)_N$ ratio of 98, versus an average of 23 for normal magmatic zircons. Normal magmatic zircons are characteristically depleted of LREE, and have an average $(Sm/La)_N$ ratio of 456; a compilation by Hoskin and Schaltegger (2003; their Fig. 3) indicates typical $(Sm/La)_N$ ratios for magmatic zircon from continental settings are ~60–550. The average $(Sm/La)_N$ ratio in Type 3 zircon is 10, reflecting enrichment in La (Fig. 10). Such low $(Sm/La)_N$ values are typically associated with zircon thought to have formed from, or been altered by, hydrothermal fluids (Hoskin et al. 1998; Whitehouse and Kamber 2002; Hoskin 2005). In summary, relative to magmatic zircons, the porous domains that define Type 3 zircon contain elevated U, LREE, Fe, Ti, Ca, Al, Cl, and S concentrations, and anomalous $(Yb/Gd)_N$ and low $(Sm/La)_N$ ratios. These compositions reflect, in part, the composition of sub-micron inclusions or residues in the pores, however several characteristics (i.e., elevated Cl, S, and LREE, low $(Sm/La)_N$) may be indicative of interaction with saline aqueous fluids.

Late stage, luminescent rim overgrowths

Luminescent rims also have distinctive geochemical features relative to normal magmatic zircons. Rims on five grains from three samples were thick enough to analyze without overlapping the primary ion beam onto other domains; the host-rocks are plagiogranites from Atlantis Massif (IODP Holes U1309D and U1309B) sampled from

crustal depths over 1 km apart. They include a discrete plagioclase-amphibole dike (~1 cm wide) intruding gabbro (U1309D-40), a quartz diorite dike (~2 cm wide) intruding olivine gabbro (U1309D-1415), and a trondjhemite dike (~2 cm wide) cut by chlorite and actinolite veins and intruding gabbro (U1309B-39). These rims are enriched in Hf, and depleted in REE and Ti relative to magmatic cores and grains from the same sample (Figs. 7, 9), and they exhibit high Yb/Gd and low Th/U ratios (Fig. 8). Perhaps the most interesting chemical feature of the luminescent rims is the uniform, low Ti concentrations (2–3.4 ppm) they contain (Fig. 7). These Ti concentrations correspond to corrected Ti-in-zircon crystallization temperatures of 615 ± 26°C (2SD) (see Sect. 'Ti-in-zircon temperature corrections'), which is below the wet granite solidus (>650°C) at low pressures (<3 kbar; Pitcher 1997) and hints at formation under water-saturated conditions.

Discussion

Zircon saturation in plagiogranites from MOR and ophiolite settings have been estimated to require <700 ppm Zr at temperatures of ~800–875°C, based on modeling the liquid line of descent from natural samples (DeLong and Chatelain 1990). Up to 1,370 ppm Zr has been reported for plagiogranite dikes in ODP Hole 1275D (Kelemen et al. 2004), and felsic veins in ODP Hole 735B have up to 1,720 ppm Zr (Dick et al. 2000); therefore the presence of zircon in these rocks is not surprising. In contrast, Zr concentrations in other rock types, including Fe–Ti oxide gabbros, can be as low as 10 s ppm Zr (Dick et al. 2000; Kelemen et al. 2004; Blackman et al. 2006; Casey et al. 2007). Zircon in these samples possibly forms from volumetrically small, late-stage, fractionated, and Zr-rich interstitial liquids. It has been estimated that the plagiogranite dikes in ODP Hole 735B could have formed from 85 to 90% fractional crystallization of MORB (Niu et al. 2002). An alternative origin for oceanic plagiogranite involves hydrous partial melting of gabbros (Koepke et al. 2007). We cannot differentiate between these models here, but from the occurrence of zircon in a variety of rock types with a wide geographic distribution it is clear that the processes leading to zircon saturation in plutonic sections of ocean crust are common at all spreading rates.

Resolving geochemical differences for zircons from different rock types is complicated by the fact that trace element concentrations for a suite of zircons from individual samples can span a significant proportion of the field defined by all samples (Fig. 9). Concentrations of elements including U, Th, and REE can vary by more than an order-of-magnitude for a suite of zircons from an individual sample (Fig. 9). Similar compositional ranges are common for zircon populations or even individual grains from continental settings (e.g., Black et al. 1986; Chen and Williams 1990; Hoskin et al. 2000; Hoskin and Schaltegger 2003). Based on the observed Hf and trace element correlations with Ti concentration, this compositional variability likely arises from extended crystallization over a range of temperatures from a fractionating melt. In spite of these large variations, gabbro-hosted (s.l.) zircons yield on-average, lower Hf and trace element concentrations and slightly higher Ti-in-zircon temperatures than zircons from oceanic plagiogranite (e.g., Figs. 7, 11a-i). Although significant overlap exists between zircon from all rock types, the geochemistry of zircons from veins in meta-ultramafic samples is generally more similar to zircon recovered from gabbroic rock types. In support of this contention is the notable lack of zircon from the veins with the elevated Hf and trace element concentrations and low Ti-in-zircon temperatures characteristic of zircon from plagiogranite. Therefore, the liquids responsible for introducing zircon to the meta-ultramafic rock are likely gabbroic and not felsic in composition. These veins are probably related to nearby gabbro plutons, and may represent gabbroic melt expelled during compaction of a cumulate mush, which was injected into surrounding mantle peridotite.

Application of corrected Ti-in-zircon temperatures

The direct application of Ti concentration to zircon crystallization temperature has been questioned recently based on a large suite of zircons from a variety of rock types from different geologic settings giving seemingly low Ti-in-zircon temperatures (Fu et al. 2008). However, the correlations between Ti and other trace elements (i.e., Hf) observed in this and other studies (e.g., Claiborne et al. 2006; Wooden et al. 2006) show that Ti-in-zircon temperatures correlate appropriately with trends expected from fractional crystallization. These observations reinforce the interpretation that Ti-substitution in zircon is largely controlled by temperature during zircon crystallization (e.g., Watson and Harrison 2005), and thus provides at least relative temperature information for suites of zircon forming in similar environments.

Ti-in-zircon temperature corrections

Corrected Ti-in-zircon crystallization temperatures (Fig. 12) are calculated using the recalibrated Ti-in-zircon equation of Ferry and Watson (2007). Based on the general absence of rutile in these samples, implying $\mathbf{a}_{TiO2}$ <1, and the observation that $\mathbf{a}_{TiO2}$ of crustal rocks (particularly those in which Ti-rich phases like ilmenite and titanite are present) is typically >0.5 (e.g., Hayden and Watson 2007),

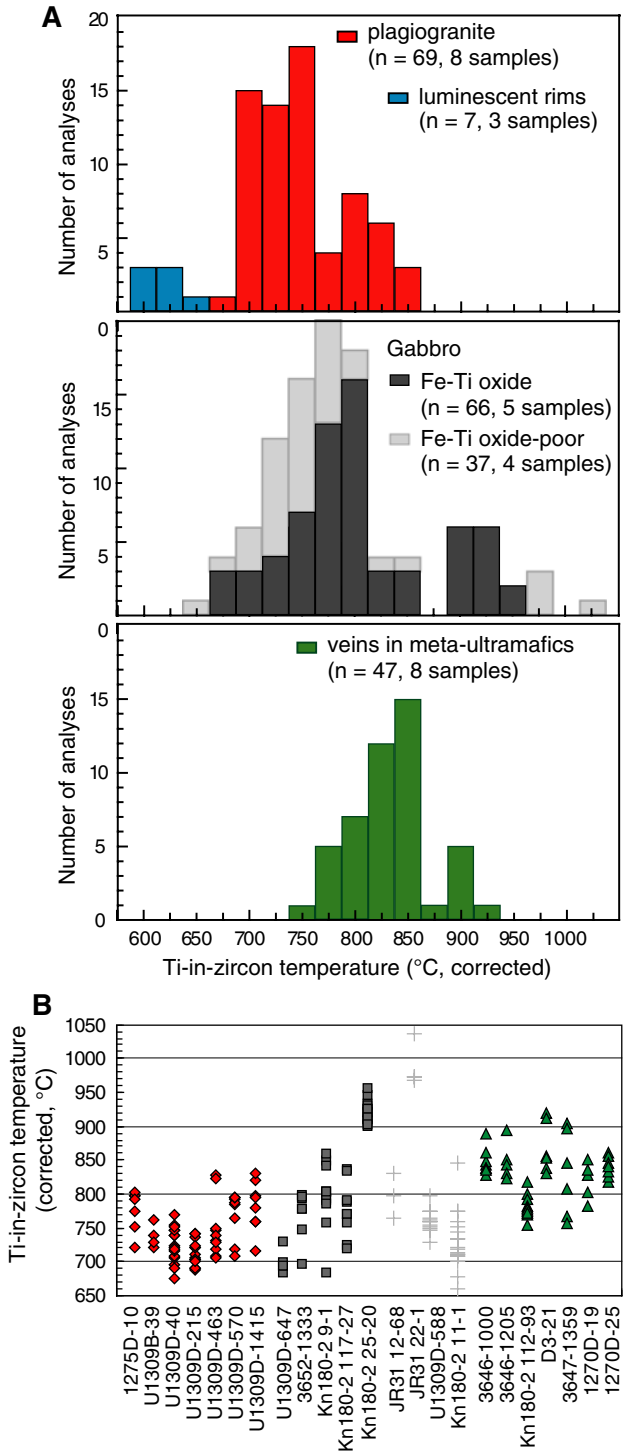

Fig. 12 Histograms showing corrected Ti-in-zircon temperatures from 226 analyses of ocean crustal zircon separated by host rock type. Temperatures were corrected assuming $\mathbf{a}_{TiO2} = 0.7$, $\mathbf{a}_{SiO2} = 1.0$, and pressure = 2 kbar (see text for details). **b** Ti-in-zircon temperatures recorded within individual samples. Each point represents an analysis (symbols: *open diamond*—plagiogranite, *filled squares*—Fe–Ti oxide gabbro, *cross*—Fe–Ti oxide-poor gabbro, *triangle*—meta-ultramafic hosts)

an intermediate $\mathbf{a}_{TiO2} = 0.7$ is assumed for samples that do not contain rutile. This value is comparable to the $\mathbf{a}_{TiO2} = 0.8$ calculated by Jöns et al. (2009) using an average TiO_2 concentration for oceanic plagiogranite, and results in an increase in calculated temperature from 30°C at 700°C, to 46° at 900°C, as compared to an assumed $\mathbf{a}_{TiO2} = 1$. Rutile inclusions were observed in two zircons from sample 1275D-10, so $\mathbf{a}_{TiO2} = 1$ was used for this sample. The inferred $\mathbf{a}_{TiO2}$ is only weakly constrained, but deviations outside a range in $\mathbf{a}_{TiO2}$ of 0.5–0.9 seem unlikely. Using an $\mathbf{a}_{TiO2}$ of 0.5 or 0.9, instead of 0.7, changes corrected temperatures by +36°/−25°C at 750°C. Quartz is commonly observed in plagiogranite samples, and occasionally as inclusions in zircon from all rock types studied. Silica activity is therefore set equal to 1, thus requiring no correction. Corrected Ti-in-zircon temperature also requires a pressure correction, since ocean crustal zircon form at pressures well below the 10 kbar pressure at which the thermometer was calibrated (Watson et al. 2006; Ferry and Watson 2007). Preliminary evaluations of pressure effects on the Ti-in-zircon thermometer suggest that there is a dependence of at least 5°C/kbar for crystallization at 750°C (e.g., Ferry and Watson 2007). Assuming that zircon crystallization takes place ~6 km beneath the ridge axis (base of average ocean crust), the pressure correction lowers Ti-in-zircon temperatures by ~40°C. Given these parameters ($\mathbf{a}_{TiO2} = 0.7$, $\mathbf{a}_{SiO2} = 1.0$, pressure = 2 kbar), the corrected temperatures change only slightly from the uncorrected temperatures, increasing by 5°C for temperatures of 900°C, and decreasing by ~10°C for temperatures of 700°C.

Ti-in zircon temperature estimates for magmatic ocean zircon

The range of corrected temperatures observed for all normal magmatic ocean zircon is 1,040–660°C (219 analyses; Supplementary Table, Fig. 12a). Sample-averaged values range from 988 ± 65°C to 699 ± 34°C (2SD). Temperatures above 960°C are recorded by only four grains from one Fe–Ti oxide-poor olivine gabbro sample JR31-22-1. There is no indication that these high Ti concentrations are erroneous (i.e., high Fe, overlap of the beam onto cracks/inclusions), and consequently sample JR31-22-1 represents the high-temperature end-member for zircon crystallization in this setting. The Ti-in-zircon temperatures recorded by zircon from both Fe–Ti oxide-poor and Fe–Ti oxide gabbro samples are widely variable (Fig. 12), spanning the entire range of observed temperatures, and give average values of 774 ± 169 and 818 ± 161°C (2SD), respectively for these rock types. Zircons from plagiogranite samples span a

narrower range (845–676°C), and record an overall lower average temperature of 750 ± 88°C (2SD; excludes luminescent rims). Zircons from veins in meta-ultramafic samples yield temperatures between 919 and 757°C with an average of 834 ± 75°C (2SD), which is consistent with previously reported average temperatures for zircons from veins in abyssal peridotite (~840°C, $n = 11$, Fu et al. 2008; ~820°C, $n = 99$, Jöns et al. 2009). The overall range of temperatures suggests that zircon crystallization can occur over a range of ~380°C in plutonic ocean crust.

Interestingly, zircons from a single sample almost ubiquitously show a span of crystallization temperatures between ~60 and 150°C (Fig. 12b), although two samples have single outliers that extend the range to 200°C (e.g., sample Kn180-2 11-1). Modeling of an average MORB melt composition suggests that after about 85% fractional crystallization the temperature of the remaining melt will be approximately 1,100°C. Thus the range of temperatures recorded by all magmatic ocean crustal zircons corresponds to crystallization of the last 10–15% of a MORB melt, comparable to the degree of fractionation estimated for the development of the plagiogranite dikes in ODP Hole 735B (Niu et al. 2002).

Solidus temperatures estimates from zircon geochemistry

The extreme enrichment in Hf and some trace elements (i.e., U, Y, REE) in zircon from oceanic plagiogranite that occurs at near constant Ti-content (Figs. 7, 9) is similar to trends observed in zircon from continental granitoid samples from the Spirit Mountain Batholith (Claiborne et al. 2006). These workers offered two potential explanations: (1) increased rate of crystallization as the system approaches eutectic-like conditions, or (2) changing partition coefficients with decreasing temperature and the build-up of water. In either case, these trends are indicative of processes occurring as a magmatic system approaches its solidus. Zircon crystallization in mafic plutonic systems occurs only very late in the differentiation history; if these enrichment trends are assumed to reflect (near) eutectic conditions, the minimum temperature at which enrichment continues serves as one estimate of the solidus temperature of the melt. Following this approach, the geochemistry of zircon from plagiogranites broadly indicates solidus temperatures between ~680 and 740°C, comparable to crystallization temperature estimates for plagioclase-amphibole dikes at Hess Deep (687–745°C; Manning et al. 1999), and felsic veins in ODP Hole 735B (525–835°C, average 674°C, $1\sigma = 77$°C; Robinson et al. 2002) determined using amphibole-plagioclase thermometry. The suite of zircons from gabbros defines a minimum temperature less clearly, but enrichment in U and to some extent Hf occurs between temperatures of >680–750°C (Fig. 9). This temperature range is ~70–150°C lower than the solidus of MAR gabbros estimated from amphibole-plagioclase thermometry (860 ± 30°C; Coogan et al. 2001) and crystallization experiments on hydrous ferrogabbro melts (~820°C; Botcharnikov et al. 2008). This discrepancy is likely indicative of continued differentiation of the most residual interstitial liquids to lower temperatures. Alternatively, the corrected Ti-in-zircon temperatures could underestimate the true crystallization temperature due to some combination of calibration uncertainties and/or factors that have not been accurately corrected for (e.g., $\mathbf{a}_{SiO2}$, $\mathbf{a}_{TiO2}$, pressure) (e.g., Fu et al. 2008).

Composition of melts in equilibrium with ocean zircon

In Fig. 11, zircon/melt partition coefficients and measured zircon REE compositions are used to model the REE composition of a melt inferred to have been in equilibrium with zircon during crystallization. Numerous studies have been conducted with the aim of determining appropriate zircon mineral/melt partition coefficients (c.f. review by Hanchar and van Westrenen 2007). Partition coefficients from Sano et al. (2002) were used here due to their close approximation to the predicted REE behavior based on lattice strain theory (Hanchar and van Westrenen 2007).

Normal magmatic zircon

The modeled melts in equilibrium with magmatic zircon from ocean crust are shown in Fig. 11a-ii. Calculated chondrite-normalized REE patterns of the equilibrium melt are smooth apart from ubiquitous Eu-anomalies, and slope gently down toward the HREE. La and Ce were excluded, due to the large uncertainties associated with low concentrations of La and the anomalous model Ce values resulting from the zircon Ce-anomaly. The shape and slope of patterns is similar for melts modeled from zircon in all rock types and geographic locations investigated. REE patterns for MOR basalts, felsic veins (plagiogranites), Fe–Ti oxide gabbros and dacite are also shown (Fig. 11a-ii) for reference, even though the gabbro and plagiogranite compositions likely do not represent liquid compositions. Five modeled melt compositions exhibit lower REE concentrations than MORB, suggesting crystallization from a more depleted source than represented by the reference lavas shown. Three of the five with the lowest concentrations come from near the 15°20′N FZ, MAR, including one plagiogranite sample from ODP Hole 1275D (1275D-10), and two from veins in serpentinized peridotite recovered in ODP Hole 1270D. The complete set of REE in zircon from this region are known only for these three samples, however Yb values reported by Grimes et al. (2007, data

repository) for several additional plagiogranite samples from ODP Hole 1275D are consistent with these low concentrations. These samples suggest that the melts producing zircon between 14°45′N and 15°45′N, MAR, were depleted in REE. Interestingly, although basalts exposed at the seafloor between 14 and 16°N are typical enriched and normal MORB (Dosso et al. 1993), peridotite in this region represents some of the most depleted ever recovered from the seafloor, and they are consistent with an unusually high degree of partial melting up to >20% (Bonatti et al. 1992; Cannat et al. 1997b; Kelemen et al. 2004; Seyler et al. 2007). The peridotite compositions have been interpreted to be the result of a two-stage melting process involving an early, high-P melting event prior to upwelling and melting beneath the ridge axis (e.g., Seyler et al. 2007). Support for this interpretation comes from Os isotopic model ages that indicate a long-term Re depletion (Brandon et al. 2000; Harvey et al. 2006). In this scenario, melt generated during upwelling beneath the ridge could be deficient in REE, because the highly incompatible REE would have been concentrated in the first melts extracted during an earlier melting event. The depleted, second-stage melts could then theoretically fractionate to produce liquids like those modeled using the composition of zircon collected near the 15°20′ FZ. Although highly speculative, this model suggests that the trace element geochemistry of ocean zircon reflects source composition. Following Grimes et al. (2007), Fig. 13a shows U versus Yb compositions of magmatic ocean crustal zircon from all zircon bearing rock types with respect to geographic location. Despite overlap, zircon from different geographic regions defines somewhat distinct fields. This plot therefore also suggests a dependence of zircon chemistry on source region composition, and in particular, that the Kane FZ (23°N MAR) and 15°20′FZ (15°N, MAR) source regions are more depleted than that surrounding the Atlantis Fracture zone (30°N) along the MAR.

Luminescent rim overgrowths and porous (Type 3) zircon

The REE patterns from the luminescent rim overgrowths and the Type 3 porous zircons differ from those in normal magmatic zircons (Fig. 11b-i). The luminescent rims have steeper patterns, whereas Type 3 (porous) zircons tend to have shallower patterns with anomalously high Nd and La. The resulting REE patterns for melts modeled using compositions of the luminescent rim overgrowths have gentle, positive slopes that are thus opposite the patterns for melts modeled using the composition of normal magmatic zircons (Fig. 11b-ii). For porous (Type 3) zircons, the modeled melt REE patterns have a generally concave-upward pattern with HREE and LREE sloping inwards toward the MREE. To a first order, these patterns suggest that the

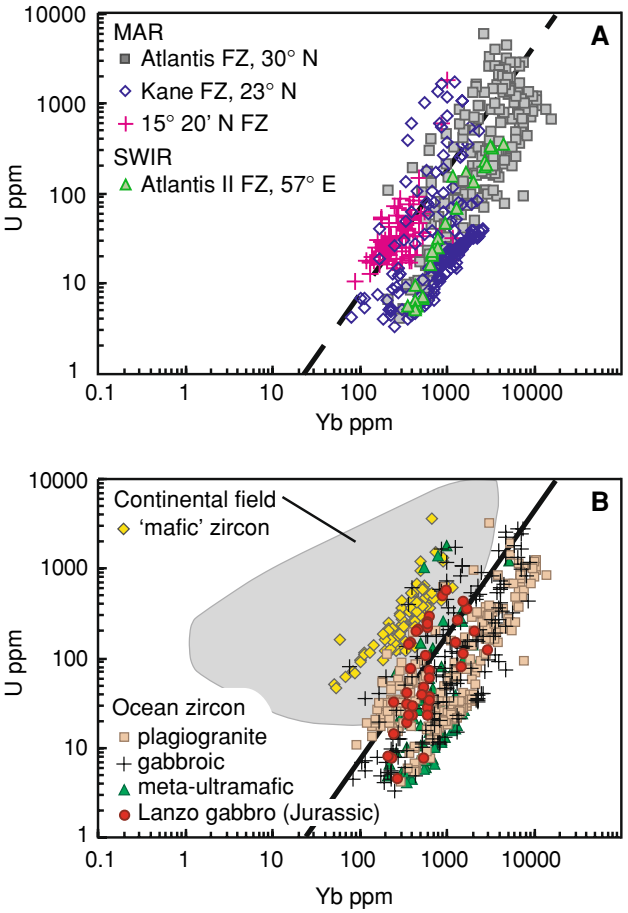

Fig. 13 **a** U versus Yb variation diagram for modern ocean crustal zircon by geographic location. Includes data listed in the Supplementary Table ($n = 356$), as well as additional data for the Kane FZ ($n = 107$) and 15°20′N FZ ($n = 59$) reported in Grimes (2008). **b** U versus Yb variation diagram for ocean crustal and continental zircon; the *bold line* denotes extremal limit of the continental zircon field (after Grimes et al. 2007). Data sources: Ocean crustal zircon: data shown in **a** ($n = 522$ analyses), and Jurassic oxide gabbro from Lanzo, Italian Alps (Kaczmarek et al. 2008); Mafic continental rocks (*diamonds*): Tertiary diorite from northern Chile (Ballard et al. 2002), Neoproterozoic and early Paleozoic metabasite from Alpine basement (Schulz et al. 2006), and unpublished data from the middle Proterozoic Duluth Gabbro (FC-1) and the late Archean Quad Creek metanorite from the Beartooth Mountains, Montana (P. Mueller and J.L. Wooden, unpublished). Approximately 20% of ocean crust zircons shown overlap with the overall continental field, requiring application of the discrimination diagrams to zircon populations (i.e., not individual grains) to evaluate provenance

luminescent rims and porous zircon formed from melts or fluids that clearly were unlike the melts from which the normal magmatic zircons crystallized.

The concave-upward patterns exhibited by melts/fluids modeled from analyses of the porous zircon are unique within the ocean zircon population. However, REE patterns with these shapes have been modeled from the latest stage rims on zircons from granitoids and high-silica rhyolites (J.L. Wooden, unpublished data), and patterns with this

shape are recognized from whole-rock analyses of some high-silica granites (e.g., Stuckless et al. 1986; Bonin et al. 1998; Stoeser and Frost 2006). Whole-rock analyses of felsic veins in ODP Hole 735B with the most enriched REE concentrations also exhibit this shape. Collectively, these observations suggest that the distinctive concave-upward pattern is indicative of highly differentiated fluids.

Development of luminescent rims and porous zircon

Luminescent rims

The luminescent CL rims share several textural and chemical features with hydrothermal zircons hosted as inclusions in hydrothermal quartz sampled from open-vein cavities in the Mole Granite (Pettke et al. 2005). Similarities include luminescence in CL, relatively high Hf concentration, low REE concentrations, and low Th/U relative to normal magmatic grains (Figs. 7, 8). Pettke et al. (2005) also report that some of the hydrothermal zircons exhibit a 'spongy' texture similar to the micro-porosity in the Type 3 zircon reported here. REE melt modeling using the Mole Granite hydrothermal zircon suite and partition coefficients from Sano et al. (2002) yields a concave-upward pattern similar to the modeled melt compositions for Type 3 ocean zircons, but distinct from the patterns modeled for luminescent rims (Fig. 11b-ii). Luminescent rims also lack the characteristically low $(Sm/La)_N$ ratios and high La concentrations reported for hydrothermal zircon (Fig. 10). Evidence for the genesis of the luminescent rims is therefore not conclusive, however based on some chemical similarities to hydrothermal zircons and average Ti-in-zircon temperature below the wet granite solidus (615 ± 26°C; 2SD) and 50–60°C lower than all other ocean crustal zircons, we conclude that the luminescent rims could have formed in an aqueous fluid-saturated environment, possibly having even precipitated from an (deuteric?) aqueous fluid.

Porous Type 3 zircon

Perturbation of original zonation and development of micro-porosity in zircon have been reported in association with alteration during high-grade metamorphism, and as a result of fluid-assisted processes resulting in solid-state partial recrystallization or local dissolution–reprecipitation re-equilibration (e.g., Hoskin and Schaltegger 2003; Geisler et al. 2007). Porosity has also been suggested to form during crystallization from, or incomplete dissolution by, low-pressure aqueous fluid (<200 MPa; Corfu et al. 2003; Bacon et al. 2007). Radiation damage is unlikely to contribute to the development of micro-porosity in the present suite of ocean crustal zircons because they are too young, and contain little U, to have acquired significant radiation damage (Ewing et al. 2003). Additionally, measured Pb/U ages from porous zircon in two different rocks collected in IODP Hole 1309D (U1309D-1175 & U1309D-1415) are within ~0.2 m.y. of normal magmatic grains from the same samples (Grimes et al. 2008), suggesting that the porous textures developed soon after crystallization of normal magmatic zircons.

The features that characterize Type 3 zircons are generally consistent with growth or alteration during aqueous fluid-assisted processes. Among these features are (1) micro-porosity (Hoskin et al. 1998; Tomaschek et al. 2003; Geisler et al. 2007), (2) LREE enrichment, steep HREE and flat LREE patterns (Hoskin et al. 1998; Hoskin and Schaltegger 2003; Whitehouse and Kamber 2002; Hoskin 2005), (3) elevated concentrations of Ca and Fe (Schaltegger 2007; Geisler et al. 2007), (4) xenotime, Th- and U-rich micro-inclusions (Geisler et al. 2007), and (5) evidence of chlorine-rich fluid inclusions. The prominent micro-porosity, inclusions, and an epitactic relationship with (unaltered relict?) cores (Fig. 5c) are consistent with fluid-assisted dissolution–reprecipitation reactions described by Geisler et al. (2007). A driving force proposed for dissolution–reprecipitation is lattice strain, caused by high concentrations of non-constituent cations initially in solid solution with zircon at higher temperatures that become meta-stable upon cooling (Geisler et al. 2007). During the dissolution–reprecipitation reaction, substituting elements are purged and the resulting zircon generally contains lower minor and trace element concentrations (Geisler et al. 2007). In the ocean crustal zircons, these purged elements are represented by the sub-micron scale inclusions enriched in Y, U, and Th that have been observed in backscattered electron images (Fig. 3c).

Chlorine concentrations up to 1,000 times higher than typical magmatic zircon (Fig. 10) imply that hydro-saline fluids were present during formation of the porous domains. If the textures observed are related to alteration, these hydro-saline fluids may have served as the catalyst for the dissolution/mobilization of existing zircon; F-rich fluids are known to mobilize Zr and other high field strength elements, leading to unequivocal hydrothermal growth of zircon (e.g., Rubin et al. 1989; Hoskin and Schaltegger 2003). Experimental studies have shown chlorine can be an effective complexing agent for LREE (Reed et al. 2000), possibly explaining the LREE enrichment associated with the porous areas.

An alternative process leading to formation of the porous zircon and apatite could involve some change during primary igneous crystallization that encouraged entrapment of fluid inclusions during zircon growth, such as the buildup of a water- or vapor-rich phase as the system approaches the magma-hydrothermal transition.

Although this possibility is difficult to rule out, based on the textural observations (i.e., perturbation of internal zoning, including individual growth zones as in Fig. 3c-iv & v); the presence of micro-inclusions is suggestive that the dissolution–reprecipitation model is the more likely explanation. However, it is considered possible that the fluids catalyzing the proposed dissolution–reprecipitation reaction were derived from the magma that crystallized the zircon originally. Following dissolution, zircon could reprecipitate essentially in situ, or within veins and along grain boundaries as observed in thin section, or perhaps even as the luminescent rim overgrowths (Fig. 4).

Comparison with zircon from continental rock types

Zircon is locally abundant in plutonic ocean crust, especially in Fe–Ti oxide-rich gabbro and plagiogranites. These rock types are widely distributed both regionally and with depth in oceanic crust; oxide-bearing gabbroic rocks and felsic differentiates make up significant portions of drilled ocean crust, including ~7% of IODP Hole 1309D (1415 meters; Blackman et al. 2006), and ~18% of ODP Hole 735B (1,508 m; Dick et al. 2000). These observations imply that ocean crust formed at a MOR and then obducted onto continental margins could serve as a potential source for detrital zircon in the sedimentary record. Additionally, textural, geochemical, and age information recorded by eclogite and ophiolite zircons has been interpreted in terms of magmatic and hydrothermal processes occurring at MORs, rather than signatures imparted during obduction at continental margins (e.g., Spandler et al. 2004; Puga et al. 2005). Therefore, the ability to distinguish ocean crustal zircons in the rock record is important.

As previously noted by Grimes et al. (2007), zircon grains from ocean crust are enriched in Y, P, and HREE and depleted in U and Th relative to zircon forming in continental settings. These workers presented several discrimination diagrams for zircon from these different settings based primarily on U and Yb concentrations, and went on to show that >4.0 Ga detrital zircons from the Jack Hills, Australia, could not have originated from magmas forming from a reservoir similar to the modern mantle. Those geochemical distinctions are supported by a further 206 analyses of zircon from the Kane FZ (Fig. 13) that were not included by Grimes et al. (2007), as well as Jurassic age ocean crustal zircon in oxide gabbro from the Lanzo massif, Italian Alps (Kaczmarek et al. 2008) (Fig. 13b). Geochemical data necessary to evaluate zircon from mafic rocks with continental or island-arc affinities on the U and Yb-based discrimination diagrams are relatively scarce within the literature. However, several published and unpublished datasets for zircon from Tertiary to Archean age continentally-derived mafic rocks are shown in Fig. 13b, and are distinct from the ocean zircon field. The discrimination is therefore effective for distinguishing zircon derived from either felsic or mafic rock types formed in these contrasting tectonic settings.

Conclusions

Zircon is a widespread accessory mineral in evolved ocean crustal rock types, exhibiting a variety of textures and large compositionally variability. Hafnium and other trace elements, including U, Th, Y, P, and HREE, vary systematically with Ti, typically showing enrichment with decreasing Ti concentration in zircon. These trends are interpreted to reflect accessory mineral fractionation (including zircon) within the crystallizing melts. Application of the Ti-in-zircon thermometer to normal magmatic zircons yields sample-averaged temperatures ranging from 988 ± 65 to 699 ± 34°C (2SD) with individual grains recording temperatures 1,040–660°C (corrected assuming $\mathbf{a}_{TiO2} = 0.7$, $\mathbf{a}_{SiO2} = 1.0$, pressure = 2 kbar), suggesting zircon growth over ~380°C in the MOR magmatic system. The overall range of crystallization temperatures, as well as protracted growth of suites of zircon from individual samples over 60–150°C in a differentiating melt contributes to large within-sample geochemical variability.

As reported in numerous studies of continental zircon populations, zircons from different rock types exhibit overlapping geochemical compositions that hinder clear distinctions. However, plagiogranite-hosted zircons have, on-average, higher Hf and trace element compositions and lower Ti-in-zircon temperatures (845–676°C; average 750 ± 88°C, 2SD) than zircon from other host-rock types. Gabbro-hosted zircons span a larger range of temperatures (1,040–660°C), and give slightly higher average values of 818 ± 161°C (2SD) for Fe–Ti oxide gabbro and 774 ± 169°C (2SD) for Fe–Ti oxide-poor gabbro. Zircons from veins in meta-ultramafic rocks and metamorphosed fault schists are most similar to gabbro-hosted zircon, recording generally lower Hf and trace element concentrations and higher Ti-in-zircon temperatures (919–757°C; average 834 ± 75°C, 2SD) than the plagiogranite zircon population. Thus, zircon in these sample probably crystallized from evolved gabbroic melts derived from nearby gabbroic plutons.

A trend of increasing Hf with decreasing Ti-in-zircon temperature is particularly well-defined by zircons from plagiogranite between ~0.7 and 2 wt% Hf. Further Hf-enrichment up to ~4.0 wt% occurs at relatively steady temperatures between ~680 and 740°C. A similar inflection is observed in plots of Ti versus U, Y, and REE and is interpreted to denote the onset of eutectic crystallization of zircon, thus providing estimated solidus

temperatures that are broadly comparable to published crystallization temperatures from plagioclase-amphibole thermometry.

Porous zircons with perturbed or chaotic CL zonation are observed in ~25% of samples examined. Porous domains have elevated La, Fe, Ca, Al, Cl, and S contents, and anomalously low $(Sm/La)_N$ ratios. These textural and geochemical characteristics are consistent with features reported for zircon formed in association with aqueous fluids. The porous grains are interpreted to reflect alteration of normal magmatic zircon, possibly via dissolution–reprecipitation catalyzed by an (deuteric?) aqueous fluid.

Overgrowth rims that are distinctly luminescent in CL yield average Ti-in-zircon temperatures of 615 ± 26°C (2SD, $n = 7$), which is ~60°C lower than nearly all other zircon analyzed here, and implies continued zircon growth below the wet-granite solidus. We propose that these rims grew near the transition between melt- and hydrothermal fluid-dominated processes, and possibly from aqueous fluids.

Zircon geochemistry reflects, in part, source location. In particular, zircon from the 15°20′FZ along the MAR exhibit low trace element compositions that distinguish them within the ocean zircon population. Additional analyses reported here are consistent with previously proposed geochemical discriminant diagrams for ocean crustal and continental zircon that are based largely on U and Yb composition. Elevated HREE coupled with low U concentrations allow effective discrimination of ~80% of all ocean crustal zircons from zircons hosted by mafic and felsic rocks formed in continental settings.

Acknowledgments We wish to thank the captains and crews the R/V Atlantis, and DSRV Alvin and Jason on the MARVEL2000 cruise, the Knorr Cruise 180-2, and the JOIDES Resolution along with shipboard parties on ODP Legs 176, 209, IODP Exp. 304/305. The authors acknowledge Henry Dick for access to samples from the SW Indian Ridge. This research used samples and data provided by the Integrated Ocean Drilling Program (IODP). Technical assistance from Brad Ito during our sessions on the SHRIMP is gratefully acknowledged. This work was supported by the National Science Foundation (OCE-0352054 and OCE-0752558 to Cheadle and John, and OCE-0550456 to John), Joint Oceanographic Institutions grants to Grimes and John, and a NASA space grant to Schwartz. We thank Peter Kelemen for early discussions of ocean zircon chemistry, and Ralf Halama and two anonymous reviewers for comments and suggestions helpful in improving this manuscript.

References

Bacon CR, Sisson TW, Mazdab FK (2007) Young cumulate complex beneath Veniamin of caldera, Aleutian arc, dated by zircon in erupted plutonic blocks. Geology 35:491–494. doi:10.1130/G23446A.1

Baines AG (2006) Geodynamic investigation of ultra-slow spreading oceanic lithosphere; Atlantis Bank and vicinity, SW Indian Ridge. Ph.D. Dissertation, University of Wyoming

Baines AG, Cheadle MJ, John BE, Schwartz JJ (2008) The rate of oceanic detachment faulting at Atlantis Bank, SW Indian Ridge. Earth Planet Sci Lett doi:10.1016/j.epsl.2008.06.013

Ballard JR, Palin MJ, Campbell IH (2002) Relative oxidation states of magmas inferred from Ce(IV)/Ce(III) in zircon: application to porphyry copper deposits of northern Chile. Contrib Mineral Petrol 144:347–364. doi:10.1007/s00410-002-0402-5

Belousova EA, Griffin WL, O'Reilly SY, Fisher NJ (2002) Igneous zircon: trace element composition as an indicator of source rock type. Contrib Mineral Petrol 143:602–622. doi:10.1007/s00410-002-0364-7

Black LP, Williams IS, Compston W (1986) Four zircon ages from one rock: the history of a 3930 Ma-old granulite from Mount Sones, Enderby Land, Antarctica. Contrib Mineral Petrol 94:427–437. doi:10.1007/BF00376336

Blackman DK, Ildefonse B, John BE, Ohara Y, Miller DJ, MacLeod CJ et al (2006) Proceedings of integrated ocean drilling program, vol 304/305. College Station. doi:10.2204/iodp.proc.304305.2006

Bonatti E, Peyve A, Kepezhinskas P, Kurentsova N, Seyler M, Skolotnev S, Udintsev G (1992) Upper mantle heterogeneity below the Mid-Atlantic Ridge, 0–15°N. J Geophys Res 97:4461–4476. doi:10.1029/91JB02838

Bonin B, Azzouni-Sekkal A, Bussy F, Ferrag S (1998) Alkali-calcic and alkaline post-orogenic (PO) granite magmatism: petrologic constraints and geodynamic settings. Lithos 45:45–70. doi:10.1016/S0024-4937(98)00025-5

Boschi C, Früh-Green GL, Delacour A, Karson JA, Kelley DS (2006) Mass transfer and fluid flow during detachment faulting and development of an oceanic core complex, Atlantis Massif (MAR 30°N). Geochem Geophys Geosyst doi:10.1029/2005GC001074

Botcharnikov RE, Koepke J, Holtz F (2008) Experimental phase relations, mineral-melt equilibria and liquid lines of descent in a hydrous ferrobasalt—implications for the Skaargaard Intrusion and other natural systems. J Petrol 49:1687–1727. doi:10.1093/petrology/egn043

Brandon AD, Snow JE, Walker RJ, Morgan JW, Mock TD (2000) 190Pt/186Os and 187Re/187Os systematics of abyssal peridotites. Earth Planet Sci Lett 177:319–335. doi:10.1016/S0012-821X(00)00044-3

Cannat M, Casey JF (1995) An ultramafic lift at the Mid-Atlantic Ridge: successive stages of magmatism in serpentinized peridotite from the 15°N region. In: Vissers RLM, Nicolas A (eds) Mantle and lower crust exposed in oceanic ridges and in ophiolites. Kluwer Academic Publishers, Dordrecht, pp 5–34

Cannat M, Chatin F, Whitechurch H, Ceuleneer G (1997a) Gabbroic rocks trapped in the upper mantle at the Mid-Atlantic Ridge. Proc Ocean Drill Prog Sci Results 153:243–264

Cannat M, Lagabrielle Y, de Coutures N, Bougault H, Casey JF, Dmitriev L, Fouquet Y (1997b) Ultramafic and gabbroic exposures at the Mid-Atlantic Ridge: Geologic mapping in the 15°N region. Tectonophysics 279:193–214. doi:10.1016/S0040-1951(97)00113-3

Casey JF, Banerji D, Zarian P (2007) Leg 179 synthesis: geochemistry, stratigraphy, and structure of gabbroic rocks drilled in ODP Hole 1105A, Southwest Indian Ridge. In: Casey JF, Miller DJ (eds) Proceedings of ocean drilling program science results, vol 179. College Station. doi:10.2973/odp.proc.sr.179.001.2007

Cavosie AJ, Kita NT, Valley JW (2009) Mantle oxygen-isotope ratio recorded in magmatic zircon from the Mid-Atlantic Ridge. Am Mineral doi:10.2138/am.2009.2982

Cheadle MJ, John B, Lusk M, Wooden J (2008) Asymmetric spreading, and the construction of oceanic crust at the Kane

oceanic core complex, vol 89, issue 53. Eos Trans American Geophysical Union, Fall Meeting 2008, abstract no. T41D-04

Chen YD, Williams IS (1990) Zircon inheritance in mafic inclusions from Bega Batholith granites, southeastern Australia: an ion microprobe study. J Geophys Res 95:17787–17796. doi:10.1029/JB095iB11p17787

Claiborne L, Miller CF, Walker BA, Wooden JL, Mazdab FK, Bea F (2006) Tracking magmatic processes through Zr/Hf ratios in rocks and Hf and Ti zoning in zircons: an example from the Spirit Mountain batholith, Nevada. Mineral Mag 70:517–543. doi:10.1180/0026461067050348

Coogan LA, Hinton RW (2006) Do the trace element compositions of detrital zircons require Hadean continental crust? Geology 34:633–636. doi:10.1130/G22737.1

Coogan LA, Wilson RN, Gillis KM, MacLeod CJ (2001) Near-solidus evolution of oceanic gabbros: Insights from amphibole geochemistry. Geochim Cosmochim Acta 65:4339–4357. doi:10.1016/S0016-7037(01)00714-1

Corfu F, Hanchar JM, Hoskin PWO, Kinney P (2003) Atlas of zircon textures. Rev Mineral Geochem 53:469–500. doi:10.2113/0530469

Cotsonika LA, Perfit MR, Smith MC, Kamenov G, Stakes D, Ridley WI, Wallace P (2005) Petrogenesis of andesites and dacites from the southern Juan de Fuca Ridge, vol 86, issue 18. Eos Trans American Geophysical Union, Fall Meeting 2005, abstract no. V13B-0551

DeLong SE, Chatelain C (1990) Trace-element constraints on accessory-phase saturation in evolved MORB magma. Earth Planet Sci Lett 101:206–215. doi:10.1016/0012-821X(90)90154-P

Dick HJB, Natland JH, Alt JC, Bach W et al (2000) A long in situ section of lower ocean crust: results of ODP Leg 176 drilling at the Southwest Indian Ridge. Earth Planet Sci Lett 179:31–51. doi:10.1016/S0012-821X(00)00102-3

Dosso L, Bougault H, Joron JL (1993) Geochemical morphology of the north Mid-Atlantic Ridge, 10–24°N, trace element isotope complementarity. Earth Planet Sci Lett 120:443–462. doi:10.1016/0012-821X(93)90256-9

Ewing RC, Meldrum A, Wang L, Weber WJ, Corrales R (2003) Radiation effects in zircon. Rev Mineral Geochem 53:215–241. doi:10.2113/0530387

Ferry JM, Watson EB (2007) New thermodynamic models and revised calibrations for the Ti-in-zircon and Zr-in-rutile thermometers. Contrib Mineral Petrol 154:429–437. doi:10.1007/s00410-007-0201-0

Fu B, Page FZ, Cavosie AJ, Fournelle J, Kita NT, Lackey JS, Wilde SA, Valley JW (2008) Ti-in-zircon thermometry: applications and limitations. Contrib Mineral Petrol. doi:10.1007/soo410-008-0281-5

Fujiwara T, Lin J, Matsumoto T, Kelemen PB, Tucholke BE, Casey JF (2003) Crustal Evolution of the mid-Atlantic Ridge near the Fifteen-Twenty Fracture Zone in the last 5 Ma. Geochem Geophys Geosyst. doi: 1029/2002GC000364

Geisler T, Schaltegger U, Tomaschek F (2007) Re-equilibration of zircon in aqueous fluids and melts. Elements 3:43–50. doi:10.2113/gselements.3.1.43

Gillis KM (1996) Rare Earth element constraints on the origin of amphibole in gabbroic rocks from Site 896, Hess Deep. Proc Ocean Drill Prog Sci Results 147:59–75

Grimes CB (2008) Duration, rates, and patterns of crustal growth at slow-spreading mid-ocean ridges: using zircon to investigate the evolution of in situ ocean crust. Ph.D. Dissertation, University of Wyoming

Grimes CB, John BE, Kelemen PB, Mazdab F, Wooden JL, Cheadle MJ, Hanghøj K, Schwartz JJ (2007) The trace element chemistry of zircons from oceanic crust: a method for distinguishing detrital zircon provenance. Geology 35:643–646. doi:10.1130/G23603A.1

Grimes CB, John BE, Cheadle MJ, Wooden JL (2008) Protracted construction of gabbroic crust at a slow-spreading ridge: constraints from $^{206}Pb/^{238}U$ zircon ages from Atlantis Massif and IODP Hole U1309D (30°N MAR). Geochem Geophys Geosyst. doi:10.1029/2008GC002063

Halden NM, Hawthorne FC, Campbell JL, Teesdale WJ, Maxwell JA, Higuchi D (1993) Chemical characterization of oscillatory zoning in overgrowths in zircon using 3 MeV μ-PIXE. Can Mineral 31:637–647

Hanchar JM, Hoskin PWO (1998) Mudtank carbonatite, Australia, zircon. Society for luminescence microscopy and spectroscopy newsletter, vol 10, pp 2–3

Hanchar JM, Miller CF (1993) Zircon zonation patterns as revealed by cathodoluminscence and backscattered electron images: implications for interpretation of complex crustal histories. Chem Geol 110:1–13. doi:10.1016/0009-2541(93)90244-D

Hanchar JM, van Westrenen W (2007) Rare earth element behavior in zircon-melt systems. Elements 3:37–42. doi:10.2113/gselements.3.1.37

Harrison TM, Blichert-Toft J, Müller W, Albarede F, Holden P, Mojsis SJ (2005) Heterogeneous Hadean hafnium: Evidence of continental crust at 4.4 to 4.5 Ga. Science 310:1947–1950. doi:10.1126/science.1117926

Harvey J, Gannoun A, Burton KW, Rogers NW, Alard O, Parkinson IJ (2006) Ancient melt extraction from the oceanic upper mantle revealed by Re–Os isotopes in abyssal peridotites from the Mid-Atlantic ridge. Earth Planet Sci Lett 244:606–621. doi:10.1016/j.epsl.2006.02.031

Hayden LA, Watson EB (2007) Rutile saturation in hydrous siliceous melts and its bearing on Ti-thermometry of quartz and zircon. Earth Planet Sci Lett 258:561–568. doi:10.1016/j.epsl.2007.04.020

Heaman LM, Bowins R, Crocket J (1990) The chemical composition of igneous zircon suites: implications for geochemical tracer studies. Geochim Cosmochim Acta 54:1597–1607. doi:10.1016/0016-7037(90)90394-Z

Hellebrand E, Moeller V, Whitehouse M, Cannat M (2007) Formation of oceanic zircons. Geochim Cosmochim Acta 71(Suppl 1):A391

Hinton RW, Upton BGJ (1991) The chemistry of zircon: variations within and between large crystals from syenite and alkali basalt xenoliths. Geochim Cosmochim Acta 55:3287–3302. doi:10.1016/0016-7037(91)90489-R

Hoskin PWO (2005) Trace-element composition of hydrothermal zircon and the alteration of Hadean zircon from the Jack Hills, Australia. Geochim Cosmochim Acta 69:637–648. doi:10.1016/j.gca.2004.07.006

Hoskin PWO, Ireland TR (2000) Rare earth element chemistry of zircon and its use as a provenance indicator. Geology 28:627–630. doi:10.1130/0091-7613(2000)28<627:REECOZ>2.0.CO;2

Hoskin PWO, Schaltegger U (2003) The composition of zircon and igneous and metamorphic petrogenesis. Rev Mineral Geochem 53:27–62. doi:10.2113/0530027

Hoskin PWO, Kinny PD, Wyborn D (1998) Chemistry of hydrothermal zircon: investigating timing and nature of water–rock interaction. In: Arehart GB, Hulston JR, Balkema AA (eds) Water rock interaction, vol 9. AA Balkema, Rotterdam, pp 545–548

Hoskin PWO, Kinny PD, Wyborn D, Chappell BW (2000) Identifying accessory mineral saturation during differentiation in granitoid magmas: an integrated approach. J Petrol 41:1365–1396. doi:10.1093/petrology/41.9.1365

Ireland TR, Williams IS (2003) Considerations in zircon geochronology by SIMS. Rev Mineral Geochem 53:215–241. doi:10.2113/0530215

John BE, Foster DA, Murphy JM, Cheadle MJ, Baines AG, Fanning M, Copeland P (2004) Determining the cooling history of in situ lower oceanic crust—Atlantis Bank, SW Indian Ridge. Earth Planet Sci Lett 222:145–160. doi:10.1016/j.epsl.2004.02.014

Jöns N, Bach W, Schroeder T (2009) Formation and alteration of plagiogranites in an ultramafic-hosted detachment fault at the Mid-Atlantic Ridge (ODP Leg 209). Contrib Mineral Petrol. doi:10.1007/s00410-008-0357-2

Kaczmarek M-A, Müntener O, Rubatto D (2008) Trace element chemistry and U–Pb dating of zircons from oceanic gabbros and their relationship with whole rock composition (Lanzo, Italian Alps). Contrib Mineral Petrol 155:295–312. doi:10.1007/s00410-007-0243-3

Kelemen PB, Kikawa E, Miller DJ et al (2004) Proceedings of ocean drilling program, initial reports 209, College Station. doi:10.2973/odp.proc.ir.209.2004

Koepke J, Berndt J, Feig ST, Holtz F (2007) The formation of SiO_2-rich melts within deep oceanic crust by hydrous partial melting of gabbros. Contrib Mineral Petrol 153:67–84. doi:10.1007/s00410-006-0135-y

Konzett J, Armstrong RA, Sweeny RJ, Compston W (1998) The timing of MARID suite metasomatism in the Kaapvaal mantle: an ion probe study of zircons from MAARID xenoliths. Earth Planet Sci Lett 160:133–145

Korotev RL (1996) A self-consistent compilation of elemental concentration data for 93 geochemical reference samples. Geostand News 20:217–245

Kreston P, Fels P, Berggren G (1975) Kimberlitic zircons—a possible aid in prospecting for kimberlite. Mineral Deposita 10:47–56

Lissenberg CJ, Rioux M, Shimizu N, Bowring SA, Mével C (2009) Zircon dating of oceanic crustal accretion. Science doi:10.1126/science.1169556

Manning CE, Weston PE, Mahon KI (1999) Rapid high-temperature metamorphism of East Pacific Rise gabbros from Hess Deep. Earth Planet Sci Lett 144:123–132

Mattinson JM (1976) Ages of zircons from the Bay of Islands ophiolite complex, western Newfoundland. Geology 4:393–394

Mazdab FK, Wooden JL (2006) Trace element analysis in zircon by ion microprobe (SHRIMP-RG): Technique and applications. Geochim Cosmochim Acta 70(Suppl 1):A405

Moeller A, Hellebrand E, Whitehouse M, Cannat M (2006) Trace elements in young oceanic zircons, vol 87, issue 52. Eos Trans American Geophysical Union, Fall Meeting 2006, abstract no. V23E-0678

Mukasa S, Ludden JN (1987) Uranium-lead isotopic ages of plagiogranites from the Troodos Ophiolite, Cyprus, and their tectonic significance. Geology 15:825–828

Nemchin AA, Whitehouse MJ, Pidgeon RT, Meyer C (2006) Oxygen isotope signature of 4.4-3.9 Ga zircons as a monitor of differentiation processes on the moon. Geochim Cosmochim Acta 70:1864–1872. doi:10.1016/j.gca.2005.12.009

Niu Y, Gilmore T, Mackie S, Greig A, Bach W (2002) Mineral chemistry, whole-rock compositions, and petrogenesis of Leg 176 gabbros: data and discussion. Proc Ocean Drill Prog Sci Results 176:1–60

Pettke T, Audétat A, Schaltegger U, Heinrich CA (2005) Magmatic-to-hydrothermal evolution in the W-Sn mineralized Mole Granite (NSW, Australia) Part II: evolving zircon and thorite trace element chemistry. Chem Geol 220:191–213

Pitcher WS (1997) The nature and origin of granites, 2nd edn. Chapman & Hall, London

Puga E, Fanning CM, Nieto JM, Díaz de Federico A (2005) Recrystallization textures in zircon generated by ocean floor metamorphism and eclogite-facies metamorphism: a cathodoluminescence and U-Pb SHRIMP study, with constraints from REE elements. Can Mineral 43:183–202

Reddy SM, Timms NE, Trimby P, Kinny PD, Buchan C, Blake K (2006) Crystal-plastic deformation of zircon: a defect in the assumption of chemical robustness. Geology 34:257–260. doi:10.1130/G22110.1

Reed MJ, Candela PA, Piccoli PM (2000) The distribution of rare earth elements between monzogranitic melt and the aqueous volatile phase in experimental investigations at 800 degrees C and 200 MPa. Contrib Mineral Petrol 140:251–262

Robinson PT, Erzinger J, Emmermann R (2002) The composition and origin of igneous and hyrothermal veins in the lower ocean crust—ODP Hole 735B, Southwest Indian Ridge. Proc ODP Sci Results 176:1–66. doi:10.2973/odp.proc.sr.176.019.2002

Rubatto D, Gebauer D (2000) Use of cathodoluminescence for U-Pb zircon dating by ion microprobe: some examples from the Western Alps. In: Page M, Barbin V, Blanc P, Ohnenstetter D (eds) Cathodoluminescence in geosciences. Springer, Berlin, pp 373–400

Rubatto D, Hermann J (2007) Experimental zircon/melt and zircon/garnet trace element partitioning and implications for the geochronology of crustal rocks. Chem Geol 241:38–61. doi:10.1016/j.chemgeo.2007.01.027

Rubin JN, Henry CD, Price JG (1989) Hydrothermal zircons and zircon overgrowths, Sierra Blanca Peaks, Texas. Am Mineral 74:865–869

Sandwell DT, Smith WHF (1997) Marine gravity anomaly from Geosat and ERS 1 satellite altimetry. J Geophys Res 102:10039–10054

Sano Y, Terada K, Fukuoka T (2002) High mass resolution ion microprobe analysis of rare earth elements in silicate glass, apatite and zircon: lack of matrix dependency. Chem Geol 184:217–230

Schaltegger U (2007) Hydrothermal zircon. Elements 3:51–79. doi:10.2113/gselements.3.1.51

Schroeder T, John BE (2004) Strain localization on an oceanic detachment fault system, Atlantis Massif, 30 degrees N, Mid-Atlantic Ridge. Geochem Geophys Geosyst 5. doi:10.1029/2004GC000728

Schulz B, Klemd R, Brätz H (2006) Host rock compositional controls on zircon trace element signatures in metabasites from the Austroalpine basement. Geochim Cosmochim Acta 70:697–710. doi:10.1016/j.gca.2005.10.001

Schwartz J, John BE, Cheadle MJ, Miranda E, Grimes CB, Wooden J, Dick HJB (2005) Inherited zircon and the magmatic construction of oceanic crust. Science 310:654–657. doi:10.1126/science.1116349

Scoates JS, Chamberlain KR (1995) Baddelyite (ZrO_2) and zircon ($ZrSiO_4$) from anorthositic rocks of the Laramie anorthosite complex, Wyoming: petrologic consequences and U-Pb age. Am Mineral 80:1317–1327

Seyler M, Lorand J-P, Dick HJB, Drouin M (2007) Pervasive melt percolation reactions in ultra-depleted refractory harzburgites at the Mid-Atlantic Ridge, 15°20′N: ODP Hole 1274A. Contrib Mineral Petrol 153:303–319

Spandler CJ, Hermann J, Rubatto D (2004) Exsolution of thortveitite, yttrialite and xenotime during low temperature recrystallization of zircon and their significance for trace element incorporation in zircon. Am Mineral 89:1795–1806

Speer JA (1982) Zircon. In Ribbe PH (ed) Orthosilicates. Rev Mineral 5:67–112

Stoeser DB, Frost CD (2006) Nd, Pb, Sr, and O isotopic characterization of Saudi Arabian Shield terranes. Chem Geol 226:163–188

Stuckless JS, Vaughn RB, Van Trump G Jr (1986) Trace-element contents of postorogenic granites of the eastern Arabian Shield, Kingdom of Saudi Arabia. USGS Open File Report USGS-OF-0:2–6

Thomas JB, Bodnar RJ, Shimizu N, Sinha AK (2002) Determination of zircon/melt trace element partition coefficients from SIMS analysis of melt inclusions in zircon. Geochim Cosmochim Acta 66:2887–2901

Tilton GR, Hopson W, Wright JE (1981) Uranium-lead isotopic ages of the Semail Ophiolite, Oman, with applications to Tethyan Ridge Tectonics. J Geophys Res 86:2763–2775

Tomaschek F, Kennedy AK, Villa IM, Lagos M, Ballhaus C (2003) Zircons from Syros, Cyclades, Greece—recrystallization and mobilization of zircon during high-pressure metamorphism. J Petrol 44:1977–2002. doi:10.1093/petrology/egg067

Valley JW, Lackey JS, Cavosie AJ, Clechenko CC, Spicuzza MJ, Basei MAS, Bindeman IN, Ferreira VP, Sial AN, King EM, Peck WH, Sinha AK, Wei CS (2005) 4.4 billion years of crustal maturation. Contrib Mineral Petrol 150:561–580. doi:10.1007/s00410-005-0025-8

Warren CJ, Parrish RR, Waters DJ, Searle MP (2005) Dating the geologic history of Oman's Semail ophiolite: insights from U-Pb geochronology. Contrib Mineral Petrol 150:403–422. doi:10.1007/s00410-005-0028-5

Watson EB, Harrison TM (1983) Zircon saturation revisited: temperature and composition effects in a variety of crustal magma types. Earth Planet Sci Lett 64:295–304

Watson EB, Harrison TM (2005) Zircon thermometer reveals minimum melting conditions on earliest Earth. Science 308:841–844. doi:10.1126/science.1110873

Watson EB, Wark DA, Thomas JB (2006) Crystallization thermometers for zircon and rutile. Contrib Mineral Petrol 151:413–433. doi:10.1007/s00410-006-0068-5

Whitehouse MJ, Kamber BS (2002) On the overabundance of light rare earth elements in terrestrial zircon and its implications for Earth's earliest magmatic differentiation. Earth Planet Sci Lett 204:333–346

Williams C, Tivey MA, Behn MD (2006) The magnetic structure of Kane Megamullion: results from marine magnetic anomalies, paleomagnetic data and thermal modeling, vol 87, issue 52. Eos Trans American Geophysical Union, Fall Meeting 2006, abstract no. T 2:03-4A

Wooden JL, Mazdab FK, Barth AP, Miller CF, Lowery LE (2006) Temperatures (Ti) and compositional characteristics of zircon: early observations using high mass resolution on the USGS-Stanford SHRIMP-RG. Geochim Cosmochim Acta 70(Suppl 1):A707